Spin-wave dynamics in a ferrimagnetic sphere

Paul H. Bryant* and Carson D. Jeffries
Department of Physics, University of California, Berkeley, California 94720
and Materials and Chemical Sciences Division, Lawrence Berkeley Laboratory, Berkeley, California 94720

Katsuhiro Nakamura†
Fukuoka Institute of Technology, Higashi-ku, Fukuoka 811-02, Japan
(Received 7 April 1988)

An experimental study is made of the interactions between spin-wave modes excited in a sphere of yttrium iron garnet by pumping the Suhl subsidiary absorption at 9.2 GHz with the dc field parallel to [111]. The dynamical behavior of the magnetization is observed under high resolution by varying two control parameters, dc field (580 Oe $< H <$ 2100 Oe) and microwave pump power (1 mW $< P <$ 200 mW). Within this parameter space quite varied behavior is found: (i) onset of the Suhl instability by excitation of a single spin-wave mode with very narrow linewidth ($<$0.5 G); (ii) when two or more modes are excited, interactions lead to auto-oscillations with a systematic dependence of frequency (10^4–10^6 Hz) on pump power these oscillations displaying period doubling to chaos; (iii) quasiperiodicity, locking, and chaos occur when three or more modes are excited; (iv) abrupt transition to wide-band power spectra (i.e., turbulence), with hysteresis; (v) irregular relaxation oscillations and aperiodic spiking behavior. A theoretical model is developed from first principles, using the plane-wave approximation and including anisotropy effects, obtaining the lowest-order nonlinear interaction terms between the excited modes. Bifurcation behavior is examined, and dynamical behavior is numerically computed and compared to the experimental data, explaining a number of features. A theory is developed regarding the nature of the experimentally observed relaxation oscillations and spiking behavior based on the interaction of "weak" and "strong" modes, and this is demonstrated in the numerical simulations.

I. INTRODUCTION

This paper is concerned with the nonlinear dynamics of interacting spin-wave modes in a single-crystal spherical sample of yttrium iron garnet (YIG) excited through microwave resonance absorption. Spinwave instabilities were first observed by Damon[1] and by Bloembergen and Wang[2] as noisy anomalous absorption which abruptly set in at a certain microwave threshold power as the resonance was more strongly driven. This phenomena has been extensively studied; for a review see Zakharov *et al.*[3] A theory of the behavior at threshold was given by Suhl[4] in 1957, who remarked, "This situation bears a certain resemblance to the turbulent state in fluid mechanics." This observation has been validated in the more recent emergence of dynamical-systems theory and a corresponding reexamination of spin-wave dynamics, both experimentally[5–12] and theoretically.[13–20]

It was predicted,[13,14] and experimentally discovered,[5] that the behavior beyond the Suhl threshold was, in some cases, a period-doubling route to deterministic chaos. Since the wavelengths of the excited spin waves are typically much shorter than the sample size, the accessible phase space is very high dimensional, yet low-dimensional behavior can be observed. This is consistent with observations on other systems, e.g., fluids, and with the conjecture of Ruelle and Takens,[21] that the dynamics of high-dimensional systems can be controlled by a low-dimensional attractor, Since the interactions in materials like YIG are known from first principles, it is of high interest to more fully compare spin-wave experiments with theoretical models.

To fix ideas on the physical system, consider a set of spins S_j on the crystal lattice of a sphere in an external magnetic field H_0, with a Hamiltonian

$$\tilde{H} = -\hbar\gamma \sum_j \mathbf{S}_j \cdot \mathbf{H}_0 - 2J \sum_{j,j'} \mathbf{S}_j \cdot \mathbf{S}_{j'} + \sum \tilde{H}_{\text{dipole-dipole}} , \quad (1)$$

where γ is the gyromagnetic ratio and J, assumed positive, is the Heisenberg nearest-neighbor exchange energy. The Zeeman interaction leads to a uniform precession (the "uniform mode") of the crystal magnetization M about H_0 at frequency $\omega_0 \equiv \gamma H_0$ and to a narrow ferromagnetic resonance absorption at $\omega_p \approx \omega_0$ when driven by a small microwave magnetic field $h(t)$ of frequency ω_p, perpendicular to H_0. The overall dispersion relation for Eq. (1) is[22]

$$\omega_{\mathbf{k}}^2 = (\gamma H_0 - \tfrac{1}{3}\omega_m + \gamma D k^2)(\gamma H_0 - \tfrac{1}{3}\omega_m + \gamma D k^2 + \omega_m \sin^2\theta_{\mathbf{k}}) \quad (2)$$

for spin waves of frequency $\omega_{\mathbf{k}}$, wave vector $\mathbf{k}$, and azimuthal angle $\theta_{\mathbf{k}}$ relative to H_0. Here, M_s is the sample magnetization, $\omega_m \equiv \gamma 4\pi M_s$, and the exchange constant $D = 2JSa^2/\hbar\gamma$.

In the present context a spin wave corresponds to a spatial variation of the spin precessional phase across the

sample. We expect spin waves to be excited in pairs, **k** and $-\mathbf{k}$, and that in the finite sample there exists standing-wave resonance modes by virtue of boundary conditions. We refer to the pairs as (standing-wave) modes. The exchange and dipolar terms in Eq. (1) provide nonlinear coupling between the uniform and spin-wave modes. One imagines the dynamics of the system to be that of a large number of coupled nonlinear oscillators, or modes. In a quantum picture one imagines the system to be represented by coupled quantum excitations, corresponding to the photons, magnons, and lattice phonons. Magnon-magnon and magnon-phonon scattering processes have been particularly well studied in YIG spheres.[23]

Suhl[4] analyzed various orders of instabilities. To review his first-order "subsidiary-absorption" case, which we study in this paper, imagine a small YIG sphere to be placed in a microwave magnetic field h at frequency $\omega_p = 2\pi \times 9.2 \times 10^9$ sec^{-1}. In an applied dc field $H_0 = \omega_p/\gamma \approx 3265$ G, with h perpendicular to H_0, there is a narrow uniform mode resonance absorption, the so-called ferromagnetic resonance. However, if the dc field is reduced to roughly half this value, the uniform mode can strongly couple to spin-wave modes, as shown in the dispersion diagram, Fig. 1(a). Spin waves at $\omega_p/2$ are parametrically pumped by the uniform mode "driver" at ω_p. At the threshold value of the driving field h_c, the power received by the spin waves just equals that lost by relaxation to the lattice at the rate $\gamma_{\mathbf{k}}$; for $h > h_c$ the spin-wave amplitude exponentially increases.

Another case of interest, "parallel pumping" with h parallel to H_0, allows direct resonant excitation of spin waves at $\omega_p/2$ by the microwave field at ω_p, without exciting the uniform mode. Still another case, "premature saturation," occurs in second order where $\omega_p \approx \omega_{\mathbf{k}} \approx \omega_0$; nonlinear dynamics for this case has been previously reported.[5]

The focus of this paper is a detailed experimental study of spin-wave dynamics for the subsidiary absorption instability with perpendicular pumping, as well as interpretation from a theoretical model. Above the threshold one or more spin-wave modes become excited; their interaction leads to a variety of interesting phenomena. The model starts from the viewpoint of microscopic scattering processes and makes a connection to the theoretical framework of nonlinear dynamics. Some new experimental results reported in Sec. II are as follows. (1) The regions and boundaries of behavior are found in a high-resolution parameter-space diagram (phase diagram) in which the dc field and the microwave pumping power are both varied. (2) In some regions of the phase diagram the Suhl threshold is characterized by abrupt hysteretic onset of wide-band chaos. (3) In other regions the Suhl threshold is apparently marked by excitation of only a single spin-wave mode. At higher powers, when a second mode is excited, low-frequency collective oscillations (autooscillations) are observed, which may show a period-doubling route to chaos. When a third mode is excited, the system may display quasiperiodic behavior (two incommensurate collective oscillations) with locking and a quasiperiodic transition to chaos. (4) Spiking and aperiodic relaxation oscillations are also found. (5) In other regions, well beyond the Suhl threshold, rather abrupt onset of wide-band noisy states is observed.

Much of this behavior is predicted by the model. The fundamental equations governing the spin-wave dynamics [Eq. (65)] are derived in Sec. III A, including effects such as interaction with the resonator and crystalline anisotropy. An analysis of the fixed points of the equations is undertaken in Sec. III B, showing the origin of the observed

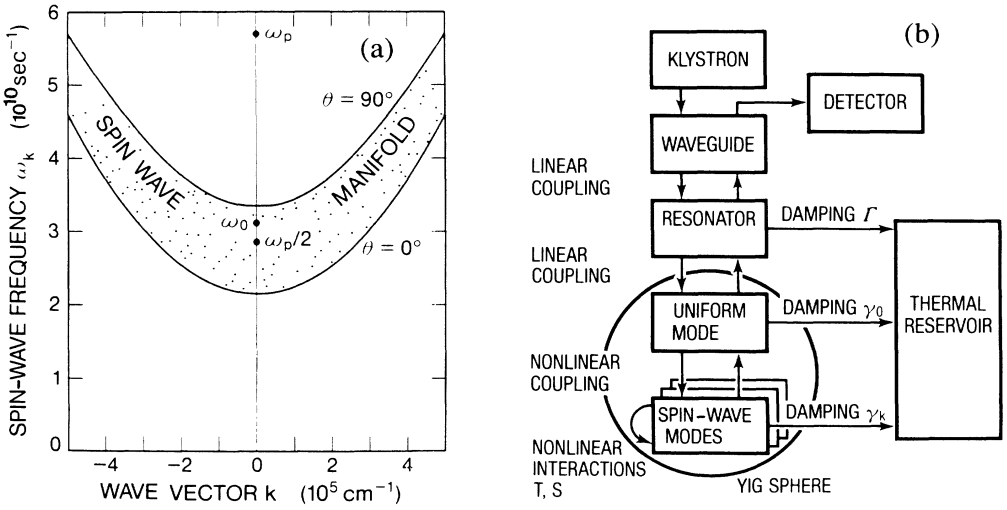

FIG. 1. (a) Spin-wave dispersion diagram, ω_k vs k, computed from Eq. (2) for YIG sphere with $H_0 = 1700$ G. The uniform mode excited by microwave pumping at ω_p can excite a pair of spin waves **k**, $-\mathbf{k}$ traveling in the azimuthal direction $\theta_{\mathbf{k}}$. (b) Schematic diagram of experimental arrangement.

hysteresis effects. A theory is presented in Sec. III C regarding the nature of relaxation oscillations and irregular spiking. These oscillations may, as is shown, provide a mechanism for *nondeterministic noise* to enter into the dynamics, even when the system seems to be operating well above the thermal background level.

The model equations are solved numerically for one, two, and three modes. These results, presented in Sec. IV, show many of the types of behavior and bifurcations observed in the experiment.

II. EXPERIMENTAL RESULTS

The experiments are performed at room temperature with a sphere of pure YIG ($Y_3Fe_5O_{12}$) having a diameter $d=0.066$ cm, spherical to within $\Delta R/R=6\times10^{-5}$ and highly polished to within 0.15 μm. YIG is a cubic insulating ferrimagnet with a Curie temperature of 559 K; its properties are reviewed by Geller.[24] The net magnetization M_s is due to the resultant of two oppositely magnetized sublattices of Fe^{3+} ions. At room temperature $4\pi M_s=1750\pm50$ G, and the exchange constant $D=5.4\times10^{-9}$ G cm^2. The Fe^{3+} ions have a ($S=\frac{5}{2}$, $L=0$) ground state, and consequently a weak interaction with the crystal lattice; the ferromagnetic resonance linewidth is $\Delta H\approx0.4$ G, limited by magnon scattering at surface imperfections.[23]

The gyromagnetic ratio $\gamma\approx1.77\times10^7$ sec^{-1} G^{-1}. In this paper the easy axis [111] was aligned parallel to the dc field H_0; for this orientation the resonance field is at a minimum.

Experimental arrangement. Figure 1(b) indicates schematically the experimental arrangement as well as elements of the theoretical model used in Sec. III. Microwave power from a klystron oscillator ($P_{max}=200$ mW) at frequency $f_p=\omega_p/2\pi=9.2$ GHz is coupled via a precision attenuator, circulator, and waveguide to a loop-gap resonator[25] containing the YIG sphere and located in a uniform and stable dc field from a large electromagnet. The resonator is centered in the waveguide with its axis parallel to the larger transverse dimension of the waveguide. It is mounted just ahead of a sliding short which can be adjusted for critical coupling to the resonator if desired. The sphere is thus subject to both a microwave field $h(t)$ and a dc field H_0, oriented with h perpendicular to H_0, which is oriented parallel to [111] except when noted. The fields are varied in the range $0<H_0<4$ kG, $0<h<5$ G. Microwave power $P_{in}\propto h^2$ incident on the resonator and YIG sphere is partially absorbed by the damping of the resonator, by the uniform mode, and the spin-wave modes, at rates Γ, γ_0, and γ_k, respectively. Power not absorbed is reflected back via the circulator to a microwave diode detector, giving a dc signal voltage S_0; the detector also gives an ac signal voltage $S(t)$ in the range 10–10^6 Hz, which is recorded and is the sample average of the real-time signal of the collective oscillations. A power spectrum of $S(t)$ from an analog spectrum analyzer (HP model 3585A) is also recorded, with an 80 dB dynamic range, free of spurious responses.

Phase diagram. Figure 2 shows the regions and boundaries of observed behavior in the parameter space (H_0, P_{in}), where H_0 is the dc field and P_{in} is the incident microwave (pump) power on a decibel scale; $P_{in}=20\log_{10}h$, where h is the relative microwave magnetic field; at $P_{in}=200$ mW, $h\approx5$ G. In regions below the line labeled "Suhl threshold" the system behaves linearly: the dc sig-

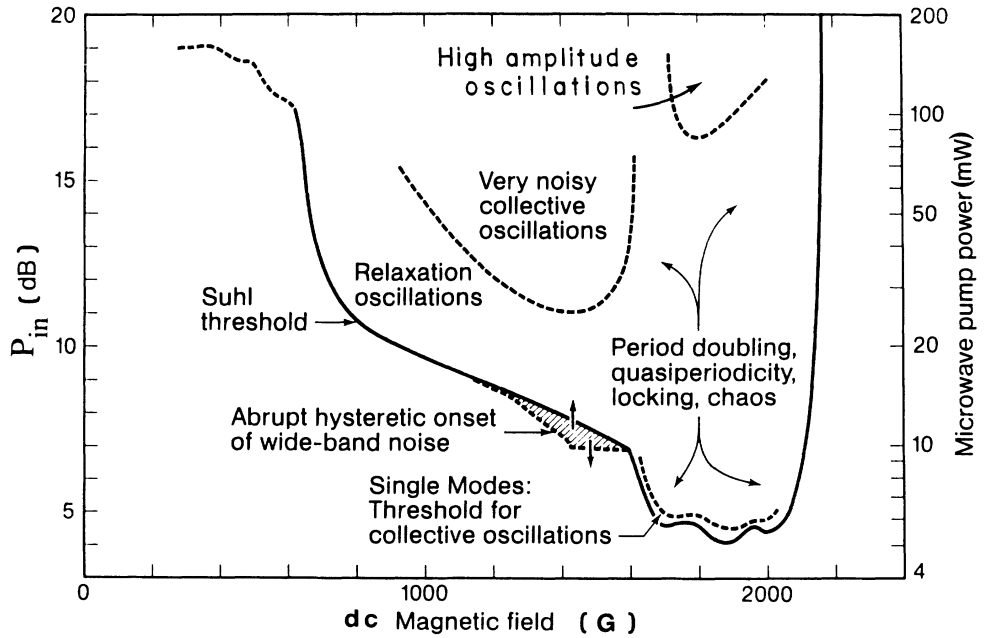

FIG. 2. Regions and boundaries of observed behavior in YIG sphere in the parameter space (H_0,P_{in}), where H_0 is the applied dc magnetic field and P_{in} (dB) the applied microwave power at $f_p=9.2$ GHz.

nal S_0 increases linearly with P_{in} and the ac signal shows only low-level wide-band detector and amplifier noise with an rms value $S_{rms} = -70$ dB (relative level). As the Suhl threshold is crossed, either by increasing P_{in} or changing H_0 in the range $600 < H_0 < 2150$ G, there is a well-defined dip in S_0. By prebalancing the detector by an additional bridge circuit, the threshold P_{in} can be determined to within 0.05 dB. As the threshold is crossed, the ac signal may also make dramatic changes depending on the region in parameter space.

Single modes. When examined under high resolution the Suhl threshold in the approximate region $1600 < H_0 < 2000$ G is seen to have a rich structure, Fig. 3(a). As the field H_0 is slowly increased at constant pump power, a series of sharp dips in the dc signal S_0 is observed, with a spacing $\Delta H_0 = 0.156$ G, which can be understood as high-order spatial resonance modes within the sphere diameter d, as first noted by Jantz and Schneider.[26] For a small change in wave vector $\Delta k = \pi/d$ at constant k in Eq. (2), the computed field change $\Delta H_0 = 2Dk\,\Delta k = 0.152$ G, using the value $k = 3\times 10^5$ cm^{-1} from Fig. 1(a) for $\theta_k = 0$. Although this elementary plane-wave calculation is in good agreement with the observed splitting, a model of spherical spin modes would be more appropriate.[27] The individual peaks show hysteresis if the sense of the field scanning is reversed.

Collective oscillations. The first few peaks in Fig. 3(a) are not accompanied by an ac signal $S(t)$, an indication that only single spin-wave modes are excited. However, as H_0 is increased, we arrive at a point where simultaneous excitation of two modes is possible due to mode overlap. Nonlinear mode-mode coupling may then result in the onset of a low frequency autooscillation signal $S(t)$ ($f_{c0} \approx 10^4 - 10^6$ Hz), e.g., Fig. 4(a). In the model, Sec. IV, this corresponds to a Hopf bifurcation to a limit cycle when two spin-wave modes are excited. These periodic collective oscillations are observed in much of the parameter space shown in Fig. 2 and display period doubling, Fig. 4(b), with sharp peaks in the power spectrum, Fig. 4(c), as large as 60 dB above the broadband baseline. [Although we are concerned in this paper primarily with the case of perpendicular pumping, similar behavior was found for parallel pumping; Fig. 4(d) shows the power spectrum for an oscillation which has successively doubled to period 8.] These oscillations may show a period-doubling cascade to chaos, Fig. 4(e), with very broad spectra peaks on a higher-level baseline, Fig. 4(f). This cascade is induced by small variations in any of the system parameters H_0, h, f_p, or crystal orientation.

Quasiperiodicity. As the magnetic field is further increased, the signal $S(t)$, e.g., Fig. 5(a), and the power spectrum $P(f)$, e.g., Fig. 5(b), give evidence for the onset of a second oscillation frequency f_2, incommensurate with the first frequency f_1. The power spectra show peaks at the combination frequencies $f_{nm} = nf_1 + mf_2$, with n,m integers; the intensities rapidly decay with increasing n,m. The frequencies are sensitively dependent on the system parameters, and are observed to lock, $f_1/f_2 \rightarrow$ rational number, and to follow a quasiperiodic route to chaos. The real-time signal, Fig. 5(c), is strikingly similar to that of two coupled pendula; Fig. 5(d) clearly shows locking. The computations of the model, Sec. IV, predict that this quasiperiodic behavior may occur when three spin-wave modes are excited. Although we cannot clearly discern on Fig. 3(a) the point where f_2 arises, it is seen nevertheless that as H_0 is further increased, more single modes are revealed, become irregularly spaced, and

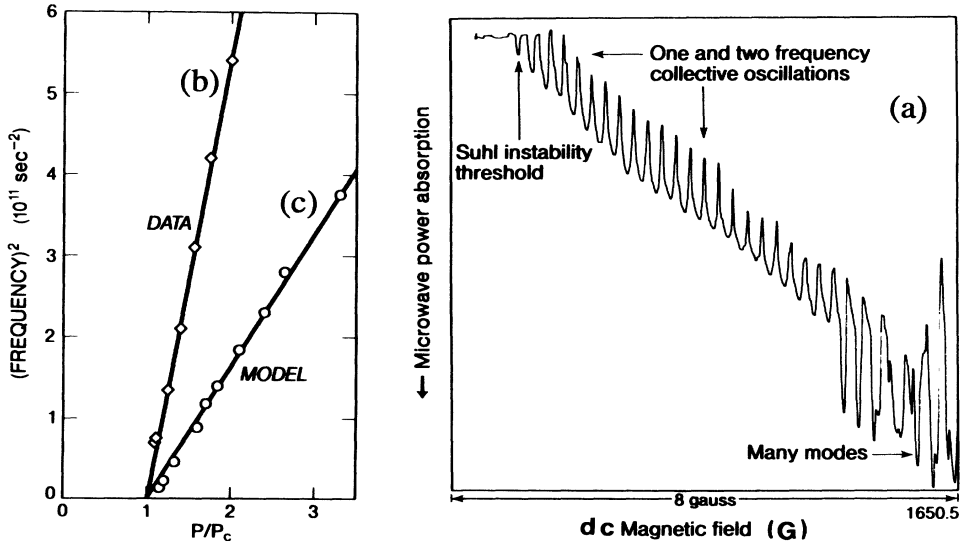

FIG. 3. (a) Single spin-wave modes from the region indicated in Fig. 2 in a YIG sphere for microwave pumping at $f_p = 9.2$ GHz. The modes are spaced by $\Delta H_0 \approx 0.156$ G. (b) Square of observed collective oscillation frequency f_{co} vs microwave pump power P_{in} relative to threshold value P_c. The solid line is a fit to the data. (c) $10 f_{co}^2$ vs P_{in}/P_c computed for model, Sec. IV; solid line is a fit to the computed points.

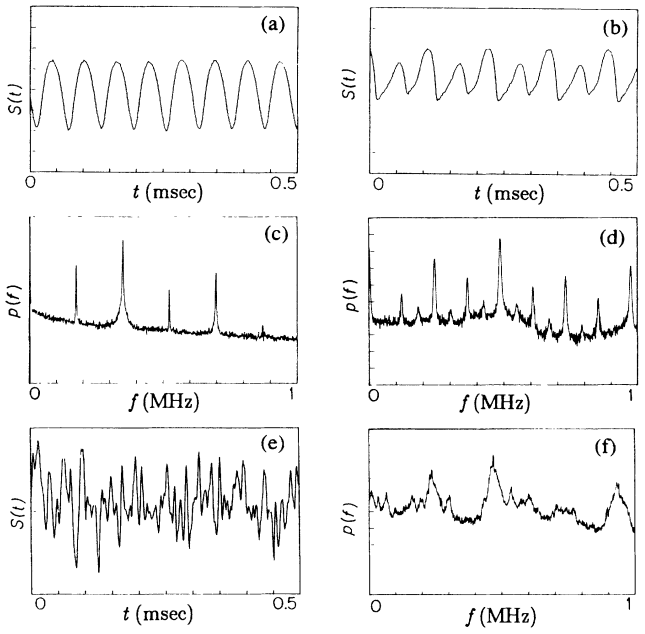

FIG. 4. (a) Observed ac signal voltage $S(t)$ of collective oscillations of spin-wave instabilities in a YIG sphere. (b) Period doubling. (c) Power spectrum of period-doubling signal, 10 dB per division. (d) Power spectrum of period-8 signal for parallel pumping case. (e) Chaotic signal. (f) Power spectrum at onset of chaos.

overlap, a situation ripe for quasiperiodicity.

Hysteretic onset of chaos. In the region $1200 \leq H_0 \leq 1600$ G in the phase diagram, Fig. 2, as the pump power P_{in} is increased, there is an abrupt onset of wide-band (deterministic) noise ($S_{\text{rms}} \approx -20$ dB), with no resolved spectral peaks. If P_{in} is decreased, this noise level persists until it reaches the lower level shown, then abruptly drops back to the level $S_{\text{rms}} = -70$ dB, normally observed below the Suhl threshold. Single modes as in Fig. 3(a) are not observed. The hysteresis itself may possibly be understood from the model, Sec. III B, as arising from subcritical symmetry-breaking bifurcations.

Aperiodic "relaxation" oscillations. Between 700 and 1200 G in Fig. 2 we find just above the Suhl threshold an aperiodic signal of the general form of Fig. 6(a), which has no resolved spectral peaks in the power spectrum, Fig. 6(b). They have a characteristic fast rise time and a slow decay time. We term these "relaxation" oscillations, although this word has been applied to a wide variety of different phenomena in the literature of spin-wave instabilities. As the pump power is increased, the times change from $\sim 10^{-2}$ to $\sim 10^{-6}$ sec. There is a fairly abrupt transition of the power spectrum of Fig. 6(c) to that of Fig. 6(d). Interspersed in these wide-band high-level oscillation regions can be found small regions in the parameter space which show periodicity, doubling, and quasiperiodicity.

High-amplitude autooscillations. At high pumping power ($P_{\text{in}} > 80$ mW), with H_0 in the range 1800–2000 G, there are high-level periodic oscillations. These are typically at least an order of magnitude greater in amplitude and frequency (typical frequency now 1 MHz) that those of the fine-structure regime. At these power levels, a large number of spin-wave modes become accessible, and the oscillations may be a cooperative effect involving many modes. Thus analysis for the interaction of only a few modes which is presented in Secs. III and IV may be of only limited applicability in this region. (However, see the analysis of Suhl and Zhang[17,19] related to this behavior.) These oscillations exhibit all of the dynamical phenomena previously described for the fine-structure regime, e.g., period doubling, quasiperiodicity, and chaos. They emerge in a Hopf bifurcation at the threshold indicated in the upper right of Fig. 2. Their emergence does not eliminate the noisy oscillations which exist below this point, however, this noise is nearly negligible compared to the oscillations when they reach full amplitude. These

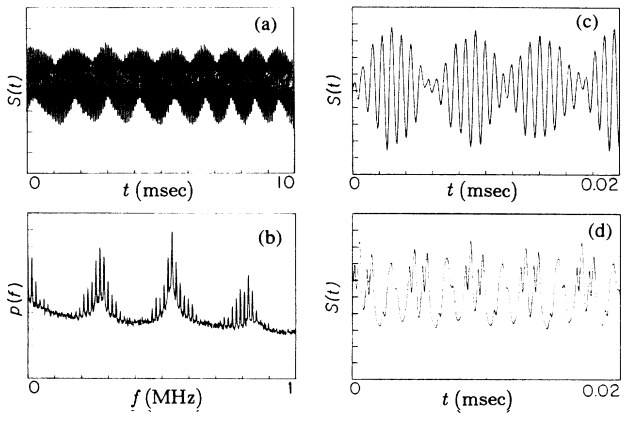

FIG. 5. (a) Observed ac signal of collective quasiperiodic oscillations of spin-wave instabilities in a YIG sphere. (b) Power spectrum of two-frequency quasiperiodic oscillations; 10 dB per division. (c) Two-frequency quasiperiodic oscillations for axis [100] parallel to H_0. (d) Frequency locking at period 14.

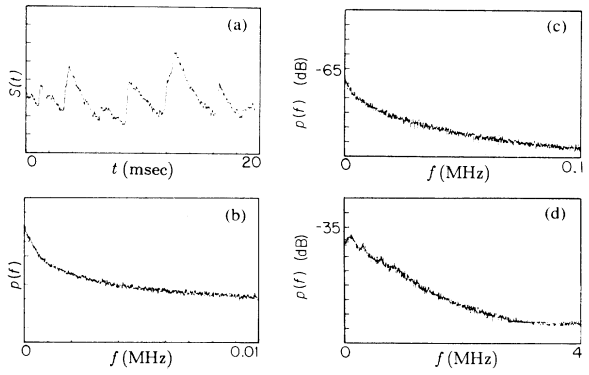

FIG. 6. (a) "Relaxation oscillations." (b) Power spectrum of relaxation oscillations; 10 dB per division. (c) Power spectrum of relaxation oscillations before transition to high-frequency noise in Fig. 2. (d) Power spectrum after transition.

high-level oscillations are also observed for parallel pumping, where they occur over a much wider range of the dc field.

Frequency of collective oscillations. The frequency f_{co} of the collective oscillations was generally observed to increase with microwave pumping power P_{in}. This could be measured over a wide frequency range in a region of parameter space near $H_0=600$ G in Fig. 2. The frequency data are plotted in Fig. 3(b) and are seen to fit the expression

$$f_{co}^2=K[(P_{in}/P_c)-1] , \tag{3}$$

where P_{in} is the pump power, P_c the value at the threshold of the oscillations, and K is a constant. Numerical results from evaluation of the model, Sec. IV, with two spin-wave modes excited, are plotted in Fig. 3(c) and also fit an expression of the form of Eq. (3). The value of K differs, however, owing to the dependence $K \propto \gamma_k^2$ on (assumed) relaxation rate. Approximate analytical models[28] also yield an expression similar to Eq. (3).

III. THEORY

This section deals with the analytical formulation of a model of spin-wave dynamics that may be useful in understanding the experimental results of Sec. II. The model equation [Eq. (65)] will be numerically iterated in Sec. IV and compared to the experimental dynamics.

A. Classical Hamiltonian formulation of the equations of motion

We now review spin-wave theory and present a semiclassical derivation of the fundamental equations governing the relevant spinwave dynamics. In this approach the classical magnetization M is considered to be an analytic function of position $\mathbf{r}$ and time t, and its dynamics are considered to be governed by its interaction with an effective field $\mathbf{H}(\mathbf{r},t)$. Suhl's original analysis of spin-wave instabilities[4] is also a semiclassical one which starts with classical equations of motion for $\mathbf{M}(\mathbf{r},t)$ and goes on to find the normal modes of the system and stability criteria for their calculation. Although this approach may be extended to obtain equations of motion for the spin waves and their mutual interactions, we take a slightly different approach here, working with the Hamiltonian for the system and utilizing many results due to Schlomann[29] and Zakharov *et al.*[3,30,31] in order to put it in the most desirable form. Much of this development has its roots in the quantum treatment of spin waves by Holstein and Primakoff,[32] in which they developed a sequence of transformations to diagonalize their spin Hamiltonian. The Hamiltonian formulation has the advantage of giving the equations of motion in their canonical form. The Hamiltonian may also be obtained in a corresponding quantum form, however, this is not necessary since the excitation levels of the experiment are usually far above the quantum regime. Damping is treated phenomenologically, by adding a linear damping term to the equations of motion for each spin-wave mode.

An effort is made to make the equations general—we consider oblique pumping, showing quite clearly the connection between parallel and perpendicular pumping in the subsidiary resonance regime. We also consider many details omitted in some earlier works such as the effects of crystalline anisotropy and interactions with the resonator or cavity used to couple the microwaves to the sample. In the analysis simple spin waves (i.e., plane waves) are used rather than the true spherical spin modes since this allows analytic solutions and gives the correct form for the equations of motion, although it can only yield approximate values for the various coupling coefficients.

We assume that we are well below the Curie temperature, so that the magnitude of the magnetization is approximately a constant, M_s, the saturation magnetization. ($4\pi M_s=1750$ G at 300 K for YIG). Thus M_x, M_y, and M_z are not all independent; it is sufficient to know just M_x and M_y. We also assume that the sample is in a sufficiently strong uniform external field so that the stable equilibrium magnetization is uniform alignment with the field along the z axis. Generally this configuration may lose stability when the sum of the external, demagnetizing, and anisotropy fields is reduced to zero. (Exchange effects are unimportant here for samples larger than about 1 μm.) For a sphere, neglecting crystalline anisotropy and exchange effects, the minimum field is $4\pi M_s/3$ (about 580 G for YIG at room temperature). Aside from anisotropy effects (which we discuss later in this section) the system processes axial symmetry, and this symmetry suggests the use of a complex representation: we define the transverse magnetization M_T as

$$M_T=M_x+iM_y . \tag{4}$$

For small amplitudes, M_x and M_y behave essentially as though they were canonically conjugate, while at higher amplitudes they deviate from this behavior. However, a weakly nonlinear transformation exists to new variables s_x and s_y which are canonically conjugate for all amplitudes. This transformation previously used by Schlomann[29] and Zakharov *et al.*[3,30,31] is essentially a classical version of the Holstein-Primakoff[32] transformation for the quantum treatment of spin waves. The transformation is

$$M_T=s(2\gamma M_s-\gamma^2 ss^*)^{1/2} , \tag{5}$$

where $s=s_x+is_y$ is a complex representation of the canonical variables s_x and s_y, γ is the gyromagnetic ratio, and s^* is the complex conjugate. (Note: in linear approximation $s \propto M_T$ and s has units of G sec$^{1/2}$.) It can be shown[30,11] that s and s^* obey the canonical equations

$$\frac{\partial s(\mathbf{r})}{\partial t}=i\frac{\delta\tilde{H}}{\delta s^*(\mathbf{r})}, \quad \frac{\partial s^*(\mathbf{r})}{\partial t}=-i\frac{\delta\tilde{H}}{\delta s(\mathbf{r})} , \tag{6}$$

where the Hamiltonian $\tilde{H}$ is obtained by expressing the total energy W as a function of $s(\mathbf{r})$ and $s^*(\mathbf{r})$ and δ signifies a functional derivative, i.e., $\delta\tilde{H}=\int[\delta\tilde{H}/\delta s(\mathbf{r})]\delta s(\mathbf{r})d^3\mathbf{r}$. [Note that the effective field $\mathbf{H}(\mathbf{r})$ is $-\delta W/\delta\mathbf{M}(\mathbf{r})$.] Equation (6) is an appropriate form for Hamilton's equations when using the complex representation of the conjugate variables s_x and s_y.

The next step is to expand s and s^* in Fourier series,

$$s=V_s^{-1/2}\sum_{\mathbf{k}} s_{\mathbf{k}} e^{i\mathbf{k}\cdot\mathbf{r}} ,$$
$$s^*=V_s^{-1/2}\sum_{\mathbf{k}} s^*_{-\mathbf{k}} e^{i\mathbf{k}\cdot\mathbf{r}} , \tag{7}$$

where V_s is the sample volume ($V_s\approx 1.51\times 10^{-4}$ cm^3 in the experiment). We now obtain Hamilton's equations in the form

$$\frac{\partial s_{\mathbf{k}}}{\partial t}=i\frac{\partial \tilde{H}}{\partial s^*_{\mathbf{k}}},\quad \frac{\partial s^*_{\mathbf{k}}}{\partial t}=-i\frac{\partial \tilde{H}}{\partial s_{\mathbf{k}}} . \tag{8}$$

[Note: if $\mathbf{k}$ was considered continuous rather than discrete then we would still have functional derivatives, i.e., $\partial s(\mathbf{k})/\partial t = i\delta\tilde{H}/\delta s^*(\mathbf{k})$.]

At this point we need to find explicit expressions for the different components of the total energy W. We will then form the Hamiltonian by expressing W in terms of $s_{\mathbf{k}}$ and $s^*_{\mathbf{k}}$.

W_0, the interaction energy with external field. The external field has an interaction energy W_0 with the magnetization of the ferromagnet given by

$$W_0=\int -[\mathbf{H}_0+\mathbf{h}(t)]\cdot\mathbf{M}\, d^3r , \tag{9}$$

where $\mathbf{H}_0$ is the dc magnetic field (oriented along the z axis) and $\mathbf{h}(t)$ is the microwave magnetic pumping field which has arbitrary orientation and frequency ω_p. We now define a transverse pumping field $h_T\equiv h_x+ih_y$ and express W_0 in terms of the constant Fourier components M_{T0} and M_{z0} and sample volume V_s,

$$W_0=-V_s(H_0+h_z)M_{z0}-\tfrac{1}{2}V_s(h_T M^*_{T0}+h^*_T M_{T0}) . \tag{10}$$

W_E, the exchange energy. The exchange field $\mathbf{H}_E$ and energy density E_E can be shown to be[33]

$$\mathbf{H}_E=\frac{D}{M_s}\nabla^2\mathbf{M},\quad E_E=\frac{D}{2M_s}\sum_i(\nabla M_i)^2 , \tag{11}$$

where D is the exchange constant ($D\approx 2JSa^2/\hbar\gamma$ G cm^2, where J is the Heisenberg exchange energy. $D\approx 5.4\times 10^{-9}$ G cm^2 for YIG). From this we obtain an expression for W_E in terms of $M_{T\mathbf{k}}$ and $M_{z\mathbf{k}}$ (the Fourier components of M_T and M_Z),

$$W_E=\frac{DV_s}{2M_s}\sum_{\mathbf{k}} k^2(M_{T\mathbf{k}}M^*_{T\mathbf{k}}+M_{z\mathbf{k}}M^*_{z\mathbf{k}}) . \tag{12}$$

Note that $M^*_{T\mathbf{k}}$ is to be interpreted as $(M_{T\mathbf{k}})^*$ not as $(M^*_T)_{\mathbf{k}}$.

W_D, the dipolar energy. For the demagnetizing field we follow the approach of Suhl[4] and treat the $k=0$ and $k\neq 0$ cases somewhat differently. For the $k=0$ case, certain sample shapes including infinite sheets, infinite rods, and spheres (or more generally ellipsoids) exhibit a uniform demagnetizing field $\mathbf{H}_{D0}$, in response to a uniform magnetization $\mathbf{M}_0$. The demagnetizing field and the magnetization are related by

$$\mathbf{H}_{D0}=-4\pi(N_xM_{x0},N_yM_{y0},N_zM_{z0}) , \tag{13}$$

where M_{x0}, M_{y0}, M_{z0} are the constant Fourier components of $\mathbf{M}$ and where N_x,N_y,N_z are the demagnetizing factors (note: these must be generalized to a tensor if the ellipsoid is not oriented with its principle axes corresponding to x, y, and z.) The demagnetizing factors satisfy $N_x+N_y+N_z=1$ and for the case of a sphere they are all equal to $\frac{1}{3}$. For the more general case of ellipsoidal samples see Osborn[34] and Stoner.[35] We define symmetric and asymmetric demagnetizing factors N_{D+} and D_{D-} as

$$N_{D+}=(N_x+N_y)/2,\quad N_{D-}=(N_x-N_y)/2 . \tag{14}$$

In the spherical case $N_{D+}=\frac{1}{3}$ and $N_{D-}=0$. The corresponding energy W_{D0} in terms of the transverse magnetization is given by

$$W_{D0}=2\pi V_s[N_{D+}M_{T0}M^*_{T0}+\tfrac{1}{2}N_{D-}(M^2_{T0}+M^{*2}_{T0}) +N_zM^2_{z0}] . \tag{15}$$

The components with $k\neq 0$ are very difficult to determine precisely for a spherical sample, but the problem becomes relatively easy if we neglect the boundary conditions. Starting with the Maxwell equation $\nabla\cdot\mathbf{B}=0$, we express $\mathbf{B}$ as $\mathbf{H}_D+\mathbf{H}_0+\mathbf{h}+4\pi\mathbf{M}$ and obtain

$$\nabla\cdot\mathbf{H}_D=-4\pi\nabla\cdot\mathbf{M} . \tag{16}$$

Expanding in Fourier components, the corresponding term in the total energy including all nonzero values for k is given by

$$W_{D\mathbf{k}}=2\pi V_s\sum_{\mathbf{k}\,(\neq 0)}\frac{|\mathbf{k}\cdot\mathbf{M}_{\mathbf{k}}|^2}{k^2} =2\pi V_s\sum_{\mathbf{k}\,(\neq 0)}\frac{1}{4k^2}|k_TM^*_{T,-\mathbf{k}}+k^*_TM_{T,\mathbf{k}}+2k_zM_{z\mathbf{k}}|^2 . \tag{17}$$

W_A, the anisotropy energy. If desired, crystalline anisotropy may be included in the analysis. Relatively simple results may be obtained if we restrict ourselves to the lowest-order contributions (order M_T^2) with the z axis corresponding to [001], [110], or [111], and the y axis corresponding to [1$\bar{1}$0] (the three orientations indicated for the z axis may be obtained by rotating about the [1$\bar{1}$0] axis). In this case it may be shown[11] that the anisotropy energy has the form

$$W_A=2\pi V_s\sum_{\mathbf{k}}[N_{A+}M_{T\mathbf{k}}M^*_{T\mathbf{k}}+\tfrac{1}{2}N_{A-}(M^2_{T\mathbf{k}}+M^{*2}_{T\mathbf{k}}] +O(M^A_{T\mathbf{k}}) , \tag{18}$$

where

$$N_{A+}=2K_1/4\pi M_s^2,\quad N_{A-}=0 \text{ for [001]} ,$$
$$N_{A+}=(-\tfrac{4}{3}K_1-\tfrac{4}{9}K_2)/4\pi M_s^2,\quad N_{A-}=0 \text{ for [111]} ,$$
$$N_{A+}=(-\tfrac{1}{2}K_1+\tfrac{1}{4}K_2)/4\pi M_s^2 ,$$
$$N_{A-}=(\tfrac{3}{2}K_1+\tfrac{1}{4}K_2)/4\pi M_s^2 \text{ for [110]} .$$

Values for the anisotropy factors K_1 and K_2 were measured by Hansen.[36,37] The notation used in Eq. (18) was

TABLE I. Anisotropy factors for YIG.

T (K)	$[100]N_{A+}$	$[111]N_{A+}$	$[110]N_{A+}$	$[110]N_{A-}$
4.2	−0.1030	0.0708	0.0246	−0.0784
77	−0.0937	0.0644	0.0223	−0.0714
295	−0.0501	0.0335	0.0125	−0.0376

chosen because of its similarity to the demagnetizing factors N_{D+} and N_{D-} appearing in Eq. (15). Note that for $\hat{\mathbf{z}}\|[001]$ or [111] the results are independent of the orientation of $\hat{\mathbf{x}}$ and $\hat{\mathbf{y}}$, although there will be difference in higher-order terms omitted in Eq. (18). Only the $\hat{\mathbf{z}}\|[110]$ case leads to a nonzero value of N_{A-}. This term breaks azimuthal symmetry and leads to elliptical rather than circular orbits for the uniform mode [as does the factor N_{D-} in Eq. (15) which results from shape anisotropy]. Values for N_{A+} and N_{A-} for YIG may be found in Table I, computed from Hansen's values for K_1 and K_2.

Now that the various contributions to the energy have been evaluated [Eqs. (10), (12), (15), (17), and (18)] we may combine them to form to obtain an expression for the Hamiltonian,

$$\tilde{H}=W_0+W_E+W_{D0}+W_{D\mathbf{k}}+W_A \ . \tag{19}$$

Naturally, we will want to express the Hamiltonian in terms of the canonical variables $s_{\mathbf{k}}$ and $s_{\mathbf{k}}^*$. This may be accomplished using

$$M_{T\mathbf{k}}=M_s\left[Y^{1/2}s_{\mathbf{k}}-\tfrac{1}{8}Y^{3/2}\sum_{\mathbf{k}_1,\mathbf{k}_2}s_{\mathbf{k}_1}s_{\mathbf{k}_2}s^*_{\mathbf{k}_1+\mathbf{k}_2-\mathbf{k}}\right]+O(s_{\mathbf{k}}^5) \tag{20}$$

and

$$M_{z\mathbf{k}}=M_s\left[\delta_{\mathbf{k}}-\tfrac{1}{2}Y\sum_{\mathbf{k}_1}s_{\mathbf{k}_1}s^*_{\mathbf{k}_1-\mathbf{k}}\right] , \tag{21}$$

where $Y\equiv 2\gamma/M_sV_s$, $\delta_{\mathbf{k}}\equiv 1$ for $\mathbf{k}=0$, and $\delta_{\mathbf{k}}\equiv 0$ for $\mathbf{k}\neq 0$. Since the resulting Hamiltonian is a lengthy expression, we break it into components as follows:

$$\tilde{H}=\text{const}+\tilde{H}_p+\tilde{H}_2+\tilde{H}_3+\tilde{H}_4+\cdots \ , \tag{22}$$

where $\tilde{H}_p$ consists of terms involving the pumping fields h_T and h_z, $\tilde{H}_2$ consists of quadratic terms in $s_{\mathbf{k}}$, $\tilde{H}_3$ of cubic terms, and $\tilde{H}_4$ quartic terms. The results are

$$\tilde{H}_p=\gamma h_z\sum_{\mathbf{k}}s^*_{\mathbf{k}}s_{\mathbf{k}}-\gamma Y^{-1/2}(h_Ts^*_0+h^*_Ts_0) \ , \tag{23}$$

$$\tilde{H}_2=\sum_{\mathbf{k}}A_{\mathbf{k}}s^*_{\mathbf{k}}s_{\mathbf{k}}+\tfrac{1}{2}(B^*_{\mathbf{k}}s_{\mathbf{k}}s_{-\mathbf{k}}+\text{c.c.}) \ , \tag{24}$$

where

$$A_{\mathbf{k}}=\gamma(H_0+Dk^2)+\omega_m\left[\delta_kN_{D+}-N_z+N_{A+}+(1-\delta_k)\frac{|k_T|^2}{2k^2}\right] , \tag{25}$$

$$B_{\mathbf{k}}=\omega_m\left[\delta_kN_{D-}+N_{A-}+(1-\delta_k)\frac{k_T^2}{2k^2}\right] , \tag{26}$$

$\omega_m=4\pi M_s\gamma$, and c.c. denotes complex conjugate,

$$\tilde{H}_3=-Y^{1/2}\sum_{\mathbf{k},\mathbf{k}_1}J^*_ks_{\mathbf{k}}s_{\mathbf{k}_1}s^*_{\mathbf{k}_1+\mathbf{k}}+\text{c.c.} \ , \tag{27}$$

where

$$J_{\mathbf{k}}=\omega_m\frac{k_zk_T}{2k^2}(1-\delta_k) \tag{28}$$

and

$$\tilde{H}_4=\tfrac{1}{8}Y\left[\sum_{k_1,k_2,k_3}(2E_{\mathbf{k}_1-\mathbf{k}_3}-Q_{\mathbf{k}_1}-Q_{\mathbf{k}_3})\times s_{\mathbf{k}_1}s_{\mathbf{k}_2}s^*_{\mathbf{k}_3}s^*_{\mathbf{k}_1+\mathbf{k}_2-\mathbf{k}_3}-(F^*_{\mathbf{k}_1}s_{\mathbf{k}_1}s_{\mathbf{k}_2}s_{\mathbf{k}_3}s^*_{\mathbf{k}_1+\mathbf{k}_2+\mathbf{k}_3}+\text{c.c.})\right] , \tag{29}$$

where

$$Q_{\mathbf{k}}=\gamma Dk^2+\omega_m\left[\delta_kN_{D+}+(1-\delta_k)\frac{|k_T|^2}{2k^2}+N_{A+}\right] , \tag{30}$$

$$E_{\mathbf{k}}=\gamma Dk^2+\omega_m\left[\delta_kN_z+(1-\delta_k)\frac{k_z^2}{k^2}\right] , \tag{31}$$

and

$$F_{\mathbf{k}}=\omega_m\left[(1-\delta_k)\frac{k_T^2}{2k^2}+\delta_kN_{D-}+N_{A-}\right] . \tag{32}$$

Note that while we have included in $\tilde{H}_4$ its dependence on the anisotropy factors N_{A+} and N_{A-}, there are additional contributions to $\tilde{H}_4$ from terms of order M_T^4 in the anisotropy energy. However, anisotropy is not very strong in pure YIG and it may be reasonable to neglect these terms in first approximation.

$\tilde{H}_2$ may be diagonalized by the Bogoliubov transformation

$$s_{\mathbf{k}}=\lambda_{\mathbf{k}}\nu_{\mathbf{k}}-\mu_{\mathbf{k}}\nu^*_{-\mathbf{k}} \ . \tag{33}$$

The coefficients $\lambda_{\mathbf{k}}$ and $\mu_{\mathbf{k}}$ are given by

$$\lambda_{\mathbf{k}}=\left[\frac{A_{\mathbf{k}}+\omega_{\mathbf{k}}}{2\omega_{\mathbf{k}}}\right]^{1/2} \tag{34}$$

and

$$\mu_{\mathbf{k}}=\frac{B_{\mathbf{k}}}{|B_{\mathbf{k}}|}\left[\frac{A_{\mathbf{k}}-\omega_{\mathbf{k}}}{2\omega_{\mathbf{k}}}\right]^{1/2} ,$$

where

$$\omega_{\mathbf{k}}\equiv(A_{\mathbf{k}}^2-|B_{\mathbf{k}}|^2)^{1/2} \tag{35}$$

is the spin-wave dispersion relation. $\lambda_{\mathbf{k}}$ and $\mu_{\mathbf{k}}$ satisfy

$$\lambda_{\mathbf{k}}^2-|\mu_{\mathbf{k}}|^2=1 \ , \tag{36}$$

which is required in order that the transformation be canonical, i.e., that Hamilton's equations give the correct equations of motion,

$$\dot{\nu}_{\mathbf{k}}=i\frac{\partial\tilde{H}}{\partial\nu_{\mathbf{k}}^*},\quad \dot{\nu}_{\mathbf{k}}^*=-i\frac{\partial\tilde{H}}{\partial\nu_{\mathbf{k}}}\ . \tag{37}$$

The Bogoliubov transformation puts the quadratic term in the desired form,

$$\tilde{H}_2=\sum_{\mathbf{k}}\omega_{\mathbf{k}}\nu_{\mathbf{k}}^*\nu_{\mathbf{k}}\ . \tag{38}$$

The pumping term now has the form

$$\tilde{H}_p=\gamma h_z\sum_{\mathbf{k}}\left[\frac{A_{\mathbf{k}}}{\omega_{\mathbf{k}}}\nu_{\mathbf{k}}^*\nu_{\mathbf{k}}-\frac{1}{2}\left[\frac{B_{\mathbf{k}}}{\omega_{\mathbf{k}}}\nu_{\mathbf{k}}^*\nu_{-\mathbf{k}}^*+\text{c.c.}\right]\right]$$
$$-\gamma Y^{-1/2}[(\lambda_0 h_T-\mu_0 h_T^*)\nu_0^*+\text{c.c.}]\ ; \tag{39}$$

note, if $N_{D-}+N_{A-}$ is negligibly small then $\lambda_0=1$ and $\mu_0=0$ and therefore $\nu_0=s_0$. The $h_z\nu_{\mathbf{k}}^*\nu_{-\mathbf{k}}^*$ term gives parallel pumping and the $h_T\nu_0^*$ term gives perpendicular pumping. The transformed cubic term is

$$\tilde{H}_3=-Y^{1/2}\sum_{\mathbf{k}_1,\mathbf{k}_2}(U_{\mathbf{k}_1,\mathbf{k}_2}\nu_{\mathbf{k}_1}\nu_{\mathbf{k}_2}\nu_{-(\mathbf{k}_1+\mathbf{k}_2)}+\text{c.c.}$$
$$+X_{\mathbf{k}_1,\mathbf{k}_2}\nu_{\mathbf{k}_1}\nu_{\mathbf{k}_2}\nu_{\mathbf{k}_1+\mathbf{k}_2}^*+\text{c.c.})\ , \tag{40}$$

where

$$U_{\mathbf{k}_1,\mathbf{k}_2}=J_{\mathbf{k}_1}\mu_{\mathbf{k}_1}^*\mu_{\mathbf{k}_2}^*\lambda_{\mathbf{k}_1+\mathbf{k}_2}-J_{\mathbf{k}_1}^*\lambda_{\mathbf{k}_1}\lambda_{\mathbf{k}_2}\mu_{\mathbf{k}_1+\mathbf{k}_2}^*\ , \tag{41}$$

$$X_{\mathbf{k}_1,\mathbf{k}_2}=J_{\mathbf{k}_1}^*\lambda_{\mathbf{k}_1}\lambda_{\mathbf{k}_2}\lambda_{\mathbf{k}_1+\mathbf{k}_2}+J_{\mathbf{k}_2}^*\mu_{\mathbf{k}_1}^*\lambda_{\mathbf{k}_2}\mu_{\mathbf{k}_1+\mathbf{k}_2}$$
$$+J_{\mathbf{k}_1+\mathbf{k}_2}^*\lambda_{\mathbf{k}_1}\mu_{\mathbf{k}_2}^*\mu_{\mathbf{k}_1+\mathbf{k}_2}-J_{\mathbf{k}_1}\mu_{\mathbf{k}_1}^*\mu_{\mathbf{k}_2}^*\mu_{\mathbf{k}_1+\mathbf{k}_2}$$
$$-J_{\mathbf{k}_2}\lambda_{\mathbf{k}_1}\mu_{\mathbf{k}_2}^*\lambda_{\mathbf{k}_1+\mathbf{k}_2}-J_{\mathbf{k}_1+\mathbf{k}_2}\mu_{\mathbf{k}_1}^*\lambda_{\mathbf{k}_2}\lambda_{\mathbf{k}_1+\mathbf{k}_2}\ . \tag{42}$$

Keeping only two-mode couping terms with slow time dependence, $\tilde{H}_4$ becomes

$$\tilde{H}_4=\sum_{\mathbf{k},\mathbf{k}'}\hat{T}_{\mathbf{k}\mathbf{k}'}\nu_{\mathbf{k}}\nu_{\mathbf{k}}^*\nu_{\mathbf{k}'}\nu_{\mathbf{k}'}^*+\tfrac{1}{2}\hat{S}_{\mathbf{k}\mathbf{k}'}\nu_{\mathbf{k}}^*\nu_{-\mathbf{k}}^*\nu_{\mathbf{k}'}\nu_{-\mathbf{k}'}\ , \tag{43}$$

where the parameters $\hat{T}_{\mathbf{k}\mathbf{k}'}$ and $\hat{S}_{\mathbf{k}\mathbf{k}'}$ may be obtained in terms of the previous parameters by substituting Eq. (33) into Eq. (29) and collecting all terms of the indicated types.

While we have found terms in $\tilde{H}_4$ which directly couple two spin-wave modes (of the same frequency) there are no such terms in $\tilde{H}_3$. $\tilde{H}_3$ is still needed, however, because the $\tilde{H}_3$ terms are much larger than the $\tilde{H}_4$ terms and there are second-order contributions from $\tilde{H}_3$ which do couple $\mathbf{k}$ and $\mathbf{k}'$. These occur through the off-resonance or virtual excitation of the modes $\mathbf{k}+\mathbf{k}'$ and $\mathbf{k}-\mathbf{k}'$. These modes will not normally have the same frequency as $\mathbf{k}$ and $\mathbf{k}'$, however, they may nevertheless be forced into a weak response at this frequency, which in turn produces a weak coupling between $\mathbf{k}$ and $\mathbf{k}'$ which may be of the same order as the terms in $\tilde{H}_4$. There are two essentially equivalent ways of dealing with problem. One approach is to explicitly determine the response of these off-resonance modes from the equations of motion. Since these modes are strongly detuned they will not behave as dynamical variables—their amplitudes may be expressed directly as a function of $\nu_{\mathbf{k}}$ and $\nu_{\mathbf{k}}'$. The second approach, which we follow here, is to introduce another canonical transformation[30] to new variables $b_{\mathbf{k}}$ and $b_{\mathbf{k}}^*$ which eliminates *all* of the cubic terms in the Hamiltonian. The appropriate transformation is

$$\nu_{\mathbf{k}}=b_{\mathbf{k}}+Y^{1/2}\sum_{\mathbf{k}'}\left[\frac{X_{\mathbf{k}',\mathbf{k}-\mathbf{k}'}b_{\mathbf{k}'}b_{\mathbf{k}-\mathbf{k}'}}{\omega_{\mathbf{k}}-\omega_{\mathbf{k}'}-\omega_{\mathbf{k}-\mathbf{k}'}}+\frac{(X_{\mathbf{k},\mathbf{k}'}^*+X_{\mathbf{k}',\mathbf{k}}^*)b_{\mathbf{k}'}^*b_{\mathbf{k}+\mathbf{k}'}}{\omega_{\mathbf{k}}+\omega_{\mathbf{k}'}-\omega_{\mathbf{k}+\mathbf{k}'}}+\frac{(U_{\mathbf{k},\mathbf{k}'}^*+U_{\mathbf{k}',\mathbf{k}}^*+U_{\mathbf{k}',-(\mathbf{k}+\mathbf{k}')}^*)b_{\mathbf{k}'}^*b_{-(\mathbf{k}'+\mathbf{k})}^*}{\omega_{\mathbf{k}}+\omega_{\mathbf{k}'}+\omega_{\mathbf{k}'+\mathbf{k}}}\right]\ . \tag{44}$$

Hamilton's equations in the $b_{\mathbf{k}}$ variables are correct through quadratic terms but deviate from the correct equations of motion by cubic terms. These errors can be canceled by adding the appropriate quartic terms to the Hamiltonian. [Note: These correction terms could be generated by adding the appropriate cubic terms to Eq. (44).] The transformation itself also generates new quartic terms and as a result $\hat{T}_{\mathbf{k}\mathbf{k}'}$ and $\hat{S}_{\mathbf{k}\mathbf{k}'}$ are "renormalized" to new values $T_{\mathbf{k}\mathbf{k}'}$ and $S_{\mathbf{k}\mathbf{k}'}$. Thus we now have

$$\tilde{H}_3=0 \tag{45}$$

and

$$\tilde{H}_4=\sum_{\mathbf{k},\mathbf{k}'}T_{\mathbf{k}\mathbf{k}'}b_{\mathbf{k}}b_{\mathbf{k}}^*b_{\mathbf{k}'}b_{\mathbf{k}'}^*+\tfrac{1}{2}S_{\mathbf{k}\mathbf{k}'}b_{\mathbf{k}}^*b_{-\mathbf{k}}^*b_{\mathbf{k}'}b_{-\mathbf{k}'}\ . \tag{46}$$

The transformation leaves the quadratic part of the Hamiltonian in diagonal form,

$$\tilde{H}_2=\sum_{\mathbf{k}}\omega_{\mathbf{k}}b_{\mathbf{k}}^*b_{\mathbf{k}}\ . \tag{47}$$

However, there are some very important consequences for the perpendicular pumping term [see Eq. (39)]. In the ν_k notation, the transverse field h_T only couples to the uniform mode ν_0 which is off resonance. This in turn couples to a spinwave pair, $\nu_{\mathbf{k}},\nu_{-\mathbf{k}}$, via terms in $\tilde{H}_3$ like $X_{\mathbf{k},-\mathbf{k}}^*\nu_{\mathbf{k}}^*\nu_{-\mathbf{k}}^*\nu_0$. In the $b_{\mathbf{k}}$ notation, however, $\tilde{H}_3$ has been eliminated to this mechanism no longer exists. Instead, we now have new terms appearing in $\tilde{H}_p$ whereby the external field couples directly to spin-wave pairs just as it does for the parallel pumping term. The important part of $\tilde{H}_p$ may now be expressed,

$$\tilde{H}_p=\sum_{\mathbf{k}}\left[-\tfrac{1}{2}\gamma h_z\frac{B_{\mathbf{k}}}{\omega_{\mathbf{k}}}-\gamma(\lambda_0 h_T-\mu_0 h_T^*)\frac{X_{\mathbf{k},-\mathbf{k}}^*}{\omega_0-2\omega_{\mathbf{k}}}\right.$$
$$\left.-\gamma(\lambda_0 h_T^*-\mu_0^* h_T)\frac{U_{0,\mathbf{k}}^*+U_{\mathbf{k},0}^*+U_{\mathbf{k},-\mathbf{k}}^*}{\omega_0+2\omega_{\mathbf{k}}}\right]b_{\mathbf{k}}^*b_{-\mathbf{k}}^*$$
$$+\text{c.c.}\ , \tag{48}$$

where we have omitted the direct coupling terms $h_T b_0 + \text{c.c.}$, since these are now unimportant for the subsidiary absorption. If we restrict our attention to the case where N_{D-} and N_{A-} are both zero, as occurs, for example, with a spherical sample with $\mathbf{H}_0$ parallel to [111] or [100], then $\lambda_0 = 1$ and $\mu_0 = 0$ and Eq. (48) simplifies to

$$\tilde{H}_p = \sum_{\mathbf{k}'} \left[-\tfrac{1}{2}\gamma h_z \frac{B_{\mathbf{k}}}{\omega_{\mathbf{k}}} - \gamma h_T \left[\frac{J_{\mathbf{k}}\lambda_{\mathbf{k}}^2 - J_{\mathbf{k}}^* \lambda_{\mathbf{k}}\mu_{\mathbf{k}}}{\omega_0 - 2\omega_{\mathbf{k}}} \right] - \gamma h_T^* \left[\frac{J_{\mathbf{k}}^* \mu_{\mathbf{k}}^2 - J_{\mathbf{k}}\lambda_{\mathbf{k}}\mu_{\mathbf{k}}}{\omega_0 + 2\omega_{\mathbf{k}}} \right] \right] b_{\mathbf{k}}^* b_{-\mathbf{k}}^* + \text{c.c.} \quad (49)$$

The first term corresponds to parallel pumping by the z component of the microwave field h_z. The second term corresponds to perpendicular pumping by the component of the transverse field with counterclockwise circular polarization. The third term corresponds to perpendicular pumping by the component with clockwise circular polarization. (This term is weak and may usually be ignored.)

Resonator dynamics. In the experimental setup, the microwave pumping field is generated by a resonator which surrounds the sample. This device serves the same purpose as a cavity, i.e., to intensify the field, and a similar analysis to that presented can be applied to that case. The resonator amplitude will be represented by R, a complex variable, chosen so that R and R^* behave as canonical variables and contribute a term $\tilde{H}_R$ to the Hamiltonian

$$\tilde{H}_R = \omega_R R^* R \ , \quad (50)$$

where ω_R is the resonant frequency. By equating the maximum field energy with $\tilde{H}_R$ we find that the field h_R is given by

$$h_R = \left[\frac{2\pi\omega_R}{V_R} \right]^{1/2} (R + R^*) \ , \quad (51)$$

where V_R is the effective volume of the resonator ($V_R \approx 2.06 \times 10^{-3}$ cm^3). Since we wish to consider oblique pumping we assume that h_R is linearly polarized, lies in the x-z plane, and makes an angle θ_R with the z axis. Thus $h_z = h_R \cos\theta_R$ and $h_T = h_R \sin\theta_R$. This may now be inserted into the expression for $\tilde{H}_p$, obtaining

$$\tilde{H}_p = \sum_{\mathbf{k}} \hat{G}_{\mathbf{k}} R b_{\mathbf{k}}^* b_{-\mathbf{k}}^* + \text{c.c.} \ , \quad (52)$$

where for the simpler case [Eq. (49)]

$$\hat{G}_k = -\tfrac{1}{2}\gamma \left[\frac{2\pi\omega_R}{V_R} \right]^{1/2} \frac{B_{\mathbf{k}}}{\omega_{\mathbf{k}}} \cos\theta_R - \gamma \left[\frac{2\pi\omega_R}{V_R} \right]^{1/2} \sin\theta_R \left[\frac{J_{\mathbf{k}}\lambda_{\mathbf{k}}^2 - J_{\mathbf{k}}^* \lambda_{\mathbf{k}}\mu_{\mathbf{k}}}{\omega_0 - 2\omega_{\mathbf{k}}} + \frac{J_{\mathbf{k}}^* \mu_{\mathbf{k}}^2 - J_{\mathbf{k}}\lambda_{\mathbf{k}}\mu_{\mathbf{k}}}{\omega_0 + 2\omega_{\mathbf{k}}} \right] . \quad (53)$$

Waveguide-resonator coupling. In the waveguide there is an incoming wave h_{in} and an outgoing wave h_{out}. For simplicity we will assume a complex representation with the amplitude of h_{in} equal to the square root of the input power P_{in}

$$h_{\text{in}} = P_{\text{in}}^{1/2} e^{i\omega_p t} \ . \quad (54)$$

Both h_{in} and h_{out} are taken to be the effective amplitude of the waves at the location of the sample. The outgoing wave h_{out} is made up of two components: h_{in} is reflected at the end of the wave guide and becomes the first component; the second component is the emission from the resonator and is assumed to be directly proportional to the resonator amplitude R,

$$h_{\text{out}} = h_{\text{in}} + i\beta R \ , \quad (55)$$

where β is a complex constant. Ignoring the weak coupling to the uniform mode, the resonator obeys the equation

$$\dot{R} = -(\Gamma_{\text{res}} + \Gamma_{\text{rad}})R + i \left[\omega_R R + \alpha h_{\text{in}} + \sum_{\mathbf{k}} \hat{G}_{\mathbf{k}}^* b_{\mathbf{k}} b_{-\mathbf{k}} \right] , \quad (56)$$

where Γ_{res} is resistive damping, Γ_{rad} is radiative damping (Γ_{res} and Γ_{rad} are both assumed real), and α is a complex coupling parameter. (Note that we have omitted the coupling term to the uniform mode, of the form $G^* b_0$, since it is of no importance if $\omega_p \neq \omega_0$. Its only effect is to slightly shift the resonant frequency and damping.) Conservation of energy determines the relationship between α, β, and Γ_{rad},

$$\Gamma_{\text{rad}} = \tfrac{1}{2}\alpha\alpha^*\omega_R \ , \quad (57)$$

$$\beta = \alpha^* \omega_R \ . \quad (58)$$

For critical coupling $h_{\text{out}} = 0$ and this implies

$$\Gamma_{\text{rad}} = \Gamma_{\text{rest}} = \tfrac{1}{2}\alpha\alpha^*\omega_R \quad (59)$$

or

$$|\alpha| = (2\Gamma_{\text{res}}/\omega_R)^{1/2} = Q^{-1/2} \ , \quad (60)$$

where Q is the quality factor of the resonator ($Q \equiv \omega_R / 2\Gamma_{\text{res}}$). $|\alpha|$ can be set to the critical value by adjusting a single experimental parameter, e.g., the sliding short at the end of the waveguide.

Elimination of resonator variable. Under certain conditions the resonator may be eliminated as a dynamical variable. The main requirement is that the damping of the resonator must be much greater than the effective damping $\gamma_{\mathbf{k}}$ for the spin-wave modes being excited. We will now change to slow variables $\bar{c}_{\mathbf{k}}$ defined by

$$b_{\mathbf{k}} = \bar{c}_{\mathbf{k}} e^{i\omega_p t/2}, \quad R = \tilde{R} e^{i\omega_p t} \ . \quad (61)$$

Assuming quasiequilibrium for the resonator ($\dot{\tilde{R}} \approx 0$) one can solve for $\tilde{R}$ in terms of the input field and spin-wave amplitudes and substitute this into the equation for $\dot{\bar{c}}_{\mathbf{k}}$, obtaining

$$\dot{\bar{c}}_{\mathbf{k}}=(-\gamma_{\mathbf{k}}+i\,\Delta\Omega_{\mathbf{k}})\bar{c}_{\mathbf{k}}-G_{\mathbf{k}}P_{\rm in}^{1/2}\bar{c}^{\,*}_{-\mathbf{k}}+i\sum_{\mathbf{k}'}[2T_{\mathbf{k}\mathbf{k}'}\,|\,\bar{c}_{\mathbf{k}'}\,|^2\bar{c}_{\mathbf{k}}+(S_{\mathbf{k}\mathbf{k}'}+R_{\mathbf{k}\mathbf{k}'})\bar{c}_{\mathbf{k}'}\bar{c}_{-\mathbf{k}'}\bar{c}^{\,*}_{-\mathbf{k}}]\ , \tag{62}$$

where

$$R_{\mathbf{k}\mathbf{k}'}=2i\hat{G}^{\,*}_{\mathbf{k}'}\hat{G}_{\mathbf{k}}/(\Gamma-i\,\Delta\Omega_R) \tag{63}$$

and

$$G_{\mathbf{k}}=\frac{2\hat{G}_{\mathbf{k}}\alpha}{\Gamma-i\,\Delta\Omega_R}\ , \tag{64}$$

with $\Gamma=\Gamma_{\rm res}+\Gamma_{\rm rad}$, $\Delta\Omega_{\mathbf{k}}=\omega_{\mathbf{k}}-\omega_p/2$, and $\Delta\Omega_R=\omega_R-\omega_p$. Assuming a standing wave so that $\bar{c}_{-\mathbf{k}}=e^{iq_{\mathbf{k}}}\bar{c}_{\mathbf{k}}$, where $q_{\mathbf{k}}$ is a real phase factor, we may transform to a new variable $c_{\mathbf{k}}\equiv\bar{c}_{\mathbf{k}}e^{iq_{\mathbf{k}}/2}$, and obtain our final form of the equation,

$$\dot{c}_{\mathbf{k}}=(-\gamma_{\mathbf{k}}+i\,\Delta\Omega_{\mathbf{k}})c_{\mathbf{k}}-G_{\mathbf{k}}P_{\rm in}^{1/2}c^{*}_{\mathbf{k}}+i\sum_{\mathbf{k}'}2T_{\mathbf{k}\mathbf{k}'}\,|\,c_{\mathbf{k}'}\,|^2c_{\mathbf{k}}+(S_{\mathbf{k}\mathbf{k}'}+R_{\mathbf{k}\mathbf{k}'})c^2_{\mathbf{k}'}c^{*}_{\mathbf{k}}\ . \tag{65}$$

This equation is the principle theoretical result and will be numerically iterated in Sec. IV.

B. Fixed points and stability

As a first step to understanding the behavior of excited spin-wave modes, we will consider the case where only one spin wave is excited. Examining Eq. (65) we find that $c_{\mathbf{k}}=0$ is always a fixed point—this is true regardless of how many spin-wave modes are excited to nonzero values. However, this fixed point need not be stable, its stability depends on the relative strength of the damping term $-\gamma_{\mathbf{k}}c_{\mathbf{k}}$ and forcing term $-G_{\mathbf{k}}P_{\rm in}^{1/2}c^{*}_{\mathbf{k}}$. An important feature to note about Eq. (65) is that there is inversion symmetry; if $c_{\mathbf{k}}(t)$ is a solution then so is $-c_{\mathbf{k}}(t)$. This is also true for arbitrarily many modes: the sign of each may be changed independently without effecting the validity of the solution. To determine the stability of the fixed point $c_{\mathbf{k}}=0$, we need only consider the linear part of the equation,

$$\dot{c}_{\mathbf{k}}=(-\gamma_{\mathbf{k}}+i\,\Delta\Omega_{\mathbf{k}})c_{\mathbf{k}}-G_{\mathbf{k}}P_{\rm in}^{1/2}c^{*}_{\mathbf{k}}\ . \tag{66}$$

Solving for the eigenvalues we find the stability condition

$$|\,M\,|>1\ \text{ for } c_{\mathbf{k}}=0 \text{ stability}\ , \tag{67}$$

where $M=(-\gamma_{\mathbf{k}}-i\,\Delta\Omega_{\mathbf{k}})/G^{*}_{\mathbf{k}}P_{\rm in}^{1/2}$. The condition $|\,M\,|=1$ corresponds to the "Suhl threshold" for the mode $\mathbf{k}$. Since $|\,M\,|$ is inversely related to input power $P_{\rm in}$, $|\,M\,|>1$ is below threshold and $|\,M\,|<1$ is above threshold. Above threshold the origin is a saddle point, as it always retains one stable eigenvalue. Immediately below threshold the origin is a stable node with two negative real eigenvalues. However, the eigenvalues may split into a conjugate pair below a lower threshold, which corresponds to a change from a stable node to a stable focus. This occurs for

$$P_{\rm in}<\Delta\Omega^2_{\mathbf{k}}/\,|\,G_k\,|^2\ .$$

We will now consider nontrivial (or nonzero) fixed points. Since we are still considering the behavior of a single mode, the equation $\dot{c}_{\mathbf{k}}=0$ [from Eq. (65)] can be put in the simple form

$$M+N\,|\,c_{\mathbf{k}}\,|^2=\frac{c^2_{\mathbf{k}}}{|\,c_{\mathbf{k}}\,|^2}=\text{point on unit circle}\ , \tag{68}$$

where $N=-i(2T_{\mathbf{k}\mathbf{k}}+S_{\mathbf{k}\mathbf{k}}+R^{*}_{\mathbf{k}\mathbf{k}})/G^{*}_{\mathbf{k}}P_{\rm in}^{1/2}$ and M is defined previously [Eq. (67)]. This equation has a simple geometrical interpretation, as shown in Fig. 7. We plot the point M and the unit circle in the complex plane. If we are below threshold then M lies outside the circle. We draw a line from the point M making an angle $\arg(N)$ with respect to the real axis. Typically this line will either miss the circle as in (a), in which case there are no nontrivial fixed points, or it will intersect the circle in two points as in (c), in which case there are two pairs of nontrivial fixed points $\pm c^{[1]}_{\mathbf{k}}$ and $\pm c^{[2]}_{\mathbf{k}}$. Nontrivial fixed points always come in pairs because of the symmetry of the equations mentioned previously. The transition between the two cases occurs when the line is just tangent to the circle. This is a saddle-node bifurcation with the saddle being the intersection point closest to M. Above the Suhl threshold M is inside the circle and there is always one intersection point as in (b). There are two possibilities for what may occur when crossing the Suhl

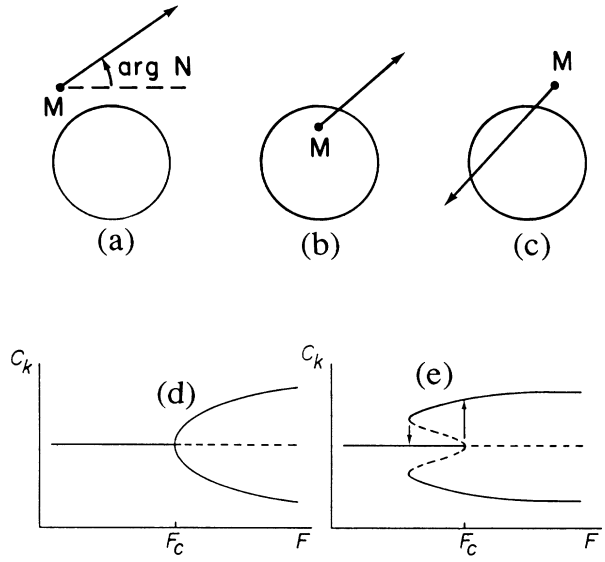

FIG. 7. Nontrivial fixed point analysis. (a) No intersections with unit circle implies no nontrivial fixed points. (b) One intersection with unit circle implies one pair of nontrivial fixed points. (c) Two intersections with unit circle implies two pairs of nontrivial fixed points. (d) Supercritical symmetry-breaking bifurcation. F is the level of forcing (pump power), F_c is the bifurcation point or Suhl threshold. Solid lines, stable fixed points; dashed lines, unstable fixed points. (e) Subcritical symmetry-breaking bifurcation, preceded by saddle-node bifurcation of nonzero fixed points. Displays hysteresis as shown.

threshold and these are illustrated in Figs. 7(d) and 7(e). In the first case, which occurs for $\mathrm{Re}(M/N)>0$, we obtain a supercritical symmetry-breaking bifurcation as a complimentary pair of stable nontrivial fixed points emerge from the origin as the origin is changing stability. The second case, which occurs for $\mathrm{Re}(M/N)<0$, involves the existence of the saddle and node below threshold. In this case we obtain a subcritical symmetry-breaking bifurcation, where the unstable nontrivial fixed points (the saddle points) converge on the origin as it changes stability. There is a hysteresis loop as shown because the system must jump from the origin to one of the stable nodes which are at finite amplitude.

In the event that R_{kk} may be neglected [i.e., it is much smaller than S_{kk} as may be the case if the resoantor damping is sufficiently large, see Eq. (63)], the type of bifurcation can be changed by changing the sign of $\Delta\Omega_k$. We find this experimentally in the region where the fine structure is observed (as mentioned previously in Sec. II) but here the hysteresis is also a very fine effect, occurring over a very small range in parameter space. However, there is a region indicated in Fig. 2 in which the hysteresis occurs over a substantial range in parameter—much more than can be attributed to a single mode. This is likely to be due to a related effect in which more than one mode is simultaneously excited.

C. Relaxation and spiking-behavior analysis

In the experiment it was observed that in certain regions aperiodic-relaxation-type oscillations are observed which are characterized by alternating fast and slow phases, where in the fast phase the amplitude of the reflected microwaves changes very rapidly and in the slow phase it changes much more gradually, typically by an order of magnitude or more [see Fig. 6(a)]. There has also been observed a related behavior pattern in which rapid spikes in the response are separated by long dormant periods of irregular length. This latter case has been the subject of much interest recently and there has been the suggestion that there may be a route to chaos by irregular periods.[20,38] We will now present a mechanism which can explain both types of behavior and discuss some of its effects on the dynamics of the experimental system.

The simplest system which can exhibit this type of behavior is a two-mode system, represented by the complex variables c_1 and c_2. The mode c_1 will be called the "strong mode;" it is assumed that the pumping level is above the Suhl threshold for this mode. The mode c_2 will be called the "weak mode;" it is assumed that the pumping level is below the Suhl threshold for this mode. In the absence of coupling between c_1 and c_2, we would expect that the origin of c_1 would be a saddle point so that this mode would be attracted to a nonzero fixed point, while the origin would be stable for c_2 so that this mode would decay to zero. However, due to intermodal coupling, the stability of the origin for c_2 can be affected by the amplitude of c_1. When coupling is included the stability criterion for $c_2=0$ is

$$\left|\frac{A+D\,|c_1|^2}{B+Fc_1^2}\right| \begin{cases} >1 & \text{stable} \\ <1 & \text{unstable}, \end{cases} \tag{69}$$

where $A=-\gamma_2-i\,\Delta\Omega_2$, $B=-G_2P_{\mathrm{in}}^{1/2}$, $D=-2iT_{2,1}$, and $F=-i(S_{2,1}+R_{2,1})$. The assumption that c_2 is below its Suhl threshold (for $c_1=0$) implies that $|A|>|B|$. There are four general cases for the behavior of the stability of c_2 as a function of c_1. Case 1: $|F|>|D|$. In this case, as $|c_1|$ is increased for any particular phase $\phi=\arg c_1$, a point is reached beyond which the denominator in Eq. (69) becomes larger in magnitude than the numerator, and stability is lost. The point of stability loss is a function of ϕ and has inversion symmetry as shown in Fig. 8(a). Case 2: $|F|<|D|$ and $K>|BF|$, where

$$K\equiv[(|A|^2-|B|^2)(|D|^2-|F|^2)]^{1/2}\mathrm{Re}\,AD^*\,.$$

In this case the point $c_2=0$ is a stable fixed point for all values of c_1 as shown in Fig. 8(b). Case 3: $|F|<|D|$ and $-|BF|<K<|BF|$. In this case there are two symmetrically located stability zones in the c_1 plane as shown in Fig. 8(c). Case 4: $|F|<|D|$ and $K<-|BF|$. This case has a annulus of instability as shown in Fig. 8(d). The general stability boundary for all four cases can be expressed as a quadratic solution,

$$|c_1|^2=\frac{-b\pm(b^2-4ac)^{1/2}}{2a}\,, \tag{70}$$

where $a=|D|^2-|F|^2$, $b=AD^*+DA^*-BF^*e^{-i\phi}-FB^*e^{i\phi}$, and $c=|A|^2-|B|^2$. Since for cases 2, 3, and 4, a and c are both positive, a solution for $|c_1|$ exists only if b is more negative than $-\sqrt{4ac}$ (in which case there are two solutions).

Now that we have analyzed the stability of the weak mode, we can proceed to explain the nature of the oscilla-

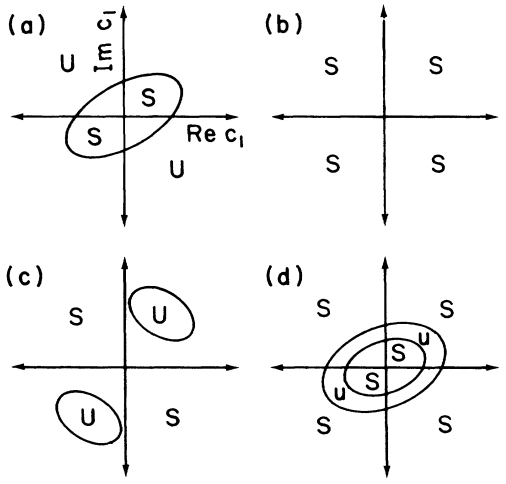

FIG. 8. Stability curve for $c_2=0$ (the weak mode) as a function of c_1 (the strong mode). S=stable, U=unstable. Four distinct cases occur as discussed in the text: (a) Case 1, (b) Case 2, (c) Case 3, (d) Case 4.

tions. We will suppose that c_1 and c_2 both start at some small but finite value. Then c_1 will increase, approaching a nontrivial fixed point and c_2 will decrease towards zero. Assuming that the nontrivial fixed point for c_1 lies in (or possibly across) a zone of instability for c_2, the phase path of c_1 will eventually enter this zone. Beyond this point c_2 will begin to increase. Under certain conditions, which we will not specify precisely but will demonstrate in Sec. IV, this can lead to a relaxation oscillation, with the fast phase occurring after c_1 reaches the instability boundary and the slow phase occurring when c_1 and c_2 both go back to values near 0. The reason that c_1 can return to a point near zero is that the origin for c_1 is a saddle point and therefore an orbit near the stable manifold may come quite close to the origin before escaping again. Orbits of the type we are describing are nearly homoclinic as they pass very close to a saddle point in the four-dimensional c_1,c_2 space. In the event that the weak mode has a focus at the origin, the orbit may be of the Silinkov type (see Guckenheimer and Holmes[39] for discussion), which is known to imply the existence of horseshoes and other complicated behavior. The distinction between relaxation oscillations and aperiodic spiking lies in the length of the dominant phase for the weak mode (examples of both are given in Sec. IV). During the dormant phase, the amplitude of c_2 decays exponentially. Consequently, a moderately long dormant phase can easily result in the amplitude of c_2 decaying to the thermal magnon level. This introduces stochasticity into the dynamics—something which might not ordinarily be expected for oscillators whose peak amplitude is many orders of magnitude above the thermal level.

IV. NUMERICAL SOLUTION OF SPIN-WAVE EQUATIONS

In order to fully explore the behavior of the spin-wave equation [Eq. (65)], it is necessary to use numerical methods, particularly when two more more interacting modes are involved. In this section we will discuss the procedures used to perform the numerical analysis and then present the results, many of which can be compared to the experimental results of Sec. II.

Each spin-wave mode is represented by a complex variable c_k which contains both amplitude and phase information for that mode. From Eq. (65), we obtain one equation for each mode, which is coupled to all other excited modes through the interaction parameters $R_{kk'}$, $S_{kk'}$, and $T_{kk'}$, and to the microwave pumping field through the parameter G_k. Our analytic results provide rough estimates for these parameters. They cannot be specified exactly from the theory for two reasons: (1) we do not know for certain which spin-wave modes in the sample are being excited and involved in the dynamics, and (2) the plane-wave approximation used in Sec. III A can yield only approximate values for the interaction parameters of the spherical modes. We typically set the spin-wave damping γ_k to 1×10^6 sec^{-1} and G_k to 1.414×10^7 W$^{-1/2}$sec^{-1}, which results in a Suhl threshold of about 5 mW as is observed experimentally in the single-mode region. $T_{kk'}$ and $S_{kk'}$ are estimated to be on the order of 10^{19} or 10^{20} G^{-2}sec^{-2}, but may vary considerably depending on which modes are involved. In order to simulate the effect of a sequence of modes as was observed experimentally, we will not assume that the modes all have zero detuning [i.e., $\Delta\Omega_k\neq0$ in Eq. (65)], but will instead choose a sequence of equally spaced values for Δf_k which will typically extend from some negative value to some positive value, where $\Delta f_k\equiv\Delta\Omega_k/2\pi$. If the excitation level is low, only those modes with detunings closest to zero will be excited. The remaining modes will be below threshold and will remain at zero amplitude. From the observed field spacing of the modes (0.16 G) we can estimate the frequency spacing using $\Delta f_{\text{mode}}\approx\gamma\,\Delta H/2\pi$, obtaining approximately 500 kHz.

In the case of excitation of a single mode alone, the analytic results of Sec. III B determine the location and stability of all fixed points. There is always at least one stable fixed point and the numerical results indicate that the system is always attracted to one of these; no periodic or chaotic attractors are observed. For appropriate parameter values hysteresis may be observed as was indicated in the theoretical treatment.

When two modes are allowed to be excited we first find periodic auto-oscillations. A particularly interesting form is observed, as shown in Figs. 9(a) and 9(b). Here mode 2 is exhibiting an asymmetric orbit while mode 1 is exhibiting a symmetrical orbit of twice the period. Symmetrical orbits are possible because of the inherent inversion symmetry of the equations. When asymmetric orbits occur they always come in complimentary pairs $[c'(t)=-c(t)]$. The nature of coupling between modes allows the type of behavior observed—since the square of c_1 appears in the equation for c_2, a change sign of c_1 (to the opposite point on the symmetric orbit) has the identical influence on c_2.

By changing the parameters we find that this orbit may undergo a bifurcation. There are many parameters which could be adjusted to accomplish this, such as power input or pump frequency, however, in Figs. 9(c) and 9(d) we have chosen to synchronously shift the detunings Δf_k of the modes. This is equivalent to shifting the value of the dc magnetic field in the experiment. (We are assuming that all modes in the sequence have identical field dependence of their frequencies.) The result is interesting: mode 1 exhibits a symmetry-breaking bifurcation while mode 2 simultaneously exhibits period doubling. Further shifting the frequencies produces a cascade of period-doubling bifurcations for both modes, leading to a chaotic orbit [Figs. 9(e) and 9(f)].

The numerical study for two modes also reveals behavior similar to the relaxation oscillations and aperiodic spiking found for the experimental system. An example of this behavior is shown in Fig. 10. The mechanism for this behavior was discussed previously in Sec. III C. There is a "strong mode" which is above its threshold, and a "weak mode" which is initially below threshold but which can become excited for brief periods when sufficient excitation is supplied via the nonlinear coupling of the strong mode. Characteristically there is a slow or dormant phase during which the weak mode is decaying

closer and closer to zero and the strong mode is changing at a relatively slow rate. At a certain critical point in the orbit of the strong mode, which is marked with an arrow in Fig. 10(a), a fast or active phase commences during which both modes [Figs. 10(a) and 10(b)] change rapidly. This is typically two or more orders of magnitude faster and also shorter in duration than the slow phase. The decay of the mode during the dormant phase may be extreme—it has been observed in some cases in the numerical study to decay by over 10 orders of magnitude. This will easily take any experimental system to the thermal level, thus introducing a stochastic element into the dynamics. Orbits with a short dormant phase tend to have the "relaxation oscillation" appearance as in Fig. 10(d) [compare to experimental Fig. 6(a)], while orbits with a long dormant phase may tend to have the "spiking" appearance, Fig. 10(c). This dormant period may become arbitrarily long for certain parameter values. This is because the orbit is approaching a saddle loop or homoclinic bifurcation which occurs when the orbit contacts the saddle point at the origin. Beyond this point a transition must occur to another attractor—typically, a nonzero fixed point for the strong mode and zero for the weak mode. It should also be noted that the relaxation and spiking behaviors do not have to be irregular—they may, for appropriate parameter values, be perfectly periodic. In some cases a cascade of period-doubling bifurcations to chaos has been observed to occur over extremely small changes in parameters ($<0.1\%$ change). This has the appearance, on first examination, as an emergence of irregularity of the orbit starting at a critical parameter value.

With three modes some new phenomena emerge. One of these is the occurrence of quasiperiodic behavior with two incommensurate frequencies. An example of this is

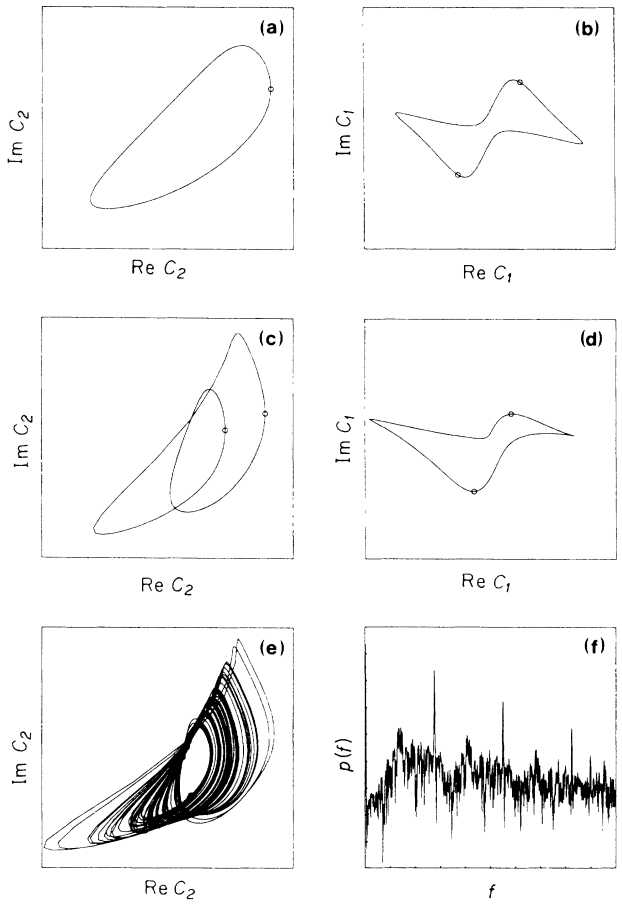

FIG. 9. Computed behavior for two modes. (a) Phase portrait for periodic oscillations, symmetric mode; $\Delta f_1 = -300$ kHz, $\Delta f_2 = 200$ kHz. (b) Symmetric mode. (c) Period doubling of asymmetric mode; $\Delta f_1 = -385$ kHz, $\Delta f_2 = 115$ kHz. (d) Symmetry breaking of symmetric mode. (e) Chaotic orbit following period-doubling cascade; $\Delta f_1 = -410$ kHz, $\Delta f_2 = 90$ kHz. (f) Power spectrum of chaotic orbit, $f_{max} = 2.5$ MHz. For all figures, $P_{in} = 0.027$ W, $\gamma_{\mathbf{k}} = 1 \times 10^6$ sec^{-1}, $G_{\mathbf{k}} = 1.414 \times 10^7$ W$^{-1/2}$ sec^{-1}, $S_{\mathbf{kk}'} = 4.078 \times 10^{19}$ G^{-2} sec^{-2} for all $\mathbf{k}$ and $\mathbf{k}'$, $T_{\mathbf{kk}'} = -1.896 \times 10^{19}$ G^{-2} sec^{-2} for $\mathbf{k} = \mathbf{k}'$ and $= 0$ for $\mathbf{k} \neq \mathbf{k}'$, and $R_{\mathbf{kk}'} = 0$ (assumed negligible) for all $\mathbf{k}$ and $\mathbf{k}'$.

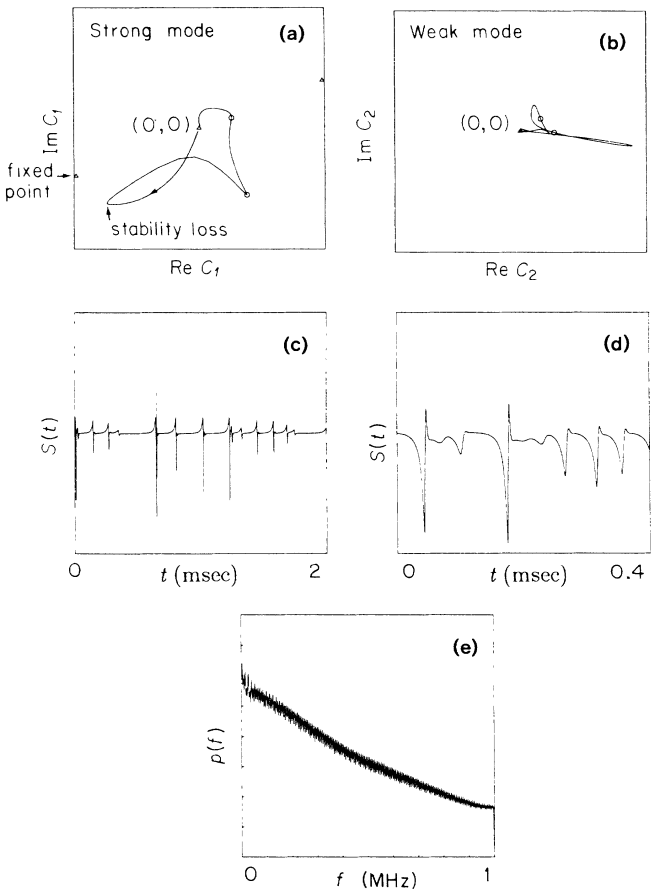

FIG. 10. (a) Aperiodic spiking; strong mode (mode 1). Arrow marks point of stability loss for weak mode (mode 2). Origin is at center of figure as indicated. $\Delta f_1 = -200$ kHz, $\Delta f_2 = 300$ kHz. (b) Weak mode. (c) Time series for aperiodic spiking behavior. (d) Time series for relaxation oscillations. $\Delta f_1 = -175$ kHz, $\Delta f_2 = 325$ kHz. (e) Fast Fourier transform for time series in (d). All figures have $P_{in} = 0.0135$ W and the other parameters are the same as in Fig. 9.

shown in Fig. 11. The three modes do not have exactly the same frequency, but rather are spaced equally in frequency by a small amount to simulate the effect of a series of modes as was observed in the experiment. Naturally, all must be very near to half of the pumping frequency, and it is the detuning which plays an important role in the dynamics. The quasiperiodic orbit lies on a two-torus in the phase space. By strobing every cycle we can make a Poincaré section of the orbit. For a quasiperiodic orbit below the transition to chaos these points all lie on a closed curve—the intersection of the two-torus with the surface of section. The section may be defined in various ways; in Fig. 11(a) the section points are the maximum value of $\mathrm{Im}c_1$ for each cycle. The orbit shown can be found to emerge from a simple periodic orbit in a Hopf bifurcation (see discussion in Guckenheimer and Holmes[39]). In the Poincaré section, the periodic orbit appears as a single point. This point spawns a circle at the bifurcation point which initially grows in size in proportion to the square root of the change in the parameter from its value at the bifurcation. While mode 1 and mode 2 (not shown) are exhibiting asymmetric orbits, mode 3 has a symmetric quasiperiodic orbit as shown in Fig. 11(b). Section points on this orbit are made simultaneously with those of mode 1. They occur twice each cycle because the basic period here is twice that of mode 1. The symmetry causes a restriction on the frequencies that appear in the spectrum. The spectrum for mode 1 is shown in Fig. 11(c). Here the allowed frequencies are all two-component harmonics of the form $f_{mn}=mf_1+nf_2$. The choice of f_1 and f_2 is not unique, but it is generally preferable to choose the two highest peaks. Figure 11(d) shows the spectrum for mode 3. Here the allowed peaks are those for which $m+n$ is odd. This can be shown to result from the symmetry of the orbit.[40]

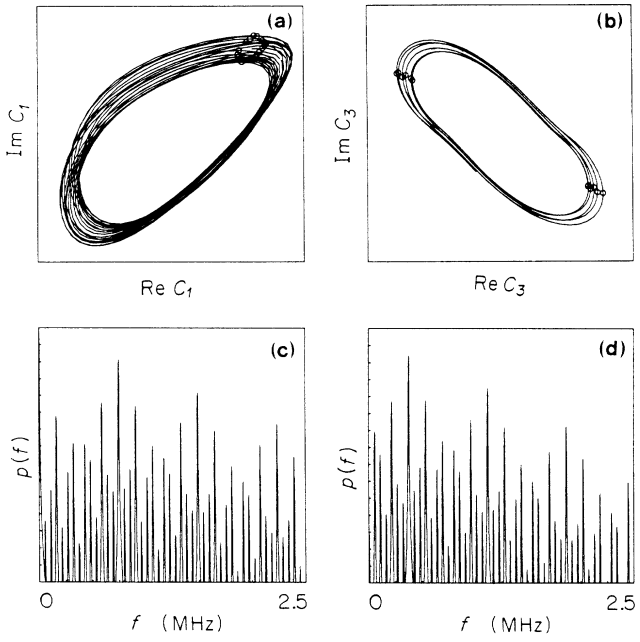

FIG. 11. Computed quasiperiodic behavior for 3 modes. (a) Mode 1 for quasiperiodic orbit, circles mark Poincaré section. (b) Mode 3: this mode exhibits a symmetrical orbit while mode 1 is asymmetrical. Mode 2 is similar to mode 1. (c) Fast Fourier transform for mode 1, vertical range 150 dB. Contains two component harmonics $f_{mn}=mf_1+nf_2$, where f_1 and f_2 may be chosen to be the largest peaks in the spectrum. (d) Fast Fourier transform for mode 3. Symmetry restricts peaks to those for which $m+n$ is odd. All figures have $P_{\mathrm{in}}=0.027$ W, $\Delta f_1=-336$ kHz, $\Delta f_2=164$ kHz, $\Delta f_3=664$ kHz, $S_{\mathbf{kk}'}=3.971\times10^{19}$ $\mathrm{G}^{-2}\mathrm{sec}^{-2}$ for $\mathbf{k}=\mathbf{k}'$ and $=4.265\times10^{19}$ $\mathrm{G}^{-2}\mathrm{sec}^{-2}$ for $\mathbf{k}\neq\mathbf{k}'$, and other parameters are the same as in Fig. 9.

By changing the parameter values away from the Hopf bifurcation point, the two-torus on which the orbit lies grows larger and becomes less smooth. At a certain critical point the orbit may become chaotic and the torus becomes fractal. This is the quasiperiodic route to chaos.[41,42] In Figs. 12(a) and 12(b) is shown a Poincaré section of such a chaotic orbit and its power spectrum. This was reached by shifting the frequencies of the three modes synchronously, to simulate the effect of shifting the dc magnetic field in the experiment. The orbit is near to a period-5 phase locking, as can be seen in the five-pointed character of the section and in the spectrum. There remain some surprisingly sharp peaks in the spectrum considering the complexity shown in the Poincaré section.

More complicated versions of the relaxation oscillations are sometimes seen for three modes (as well as the

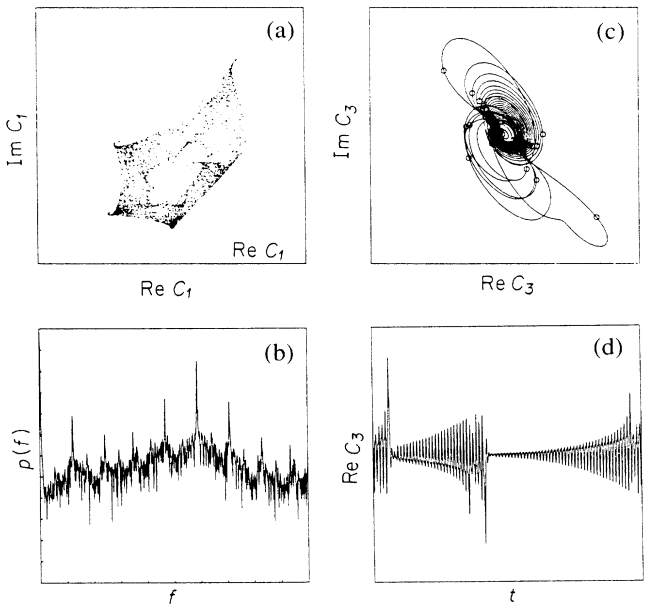

FIG. 12. (a) Poincaré section of chaotic orbit, following quasiperiodic transition to chaos. Proximity to period-5 locking produces five points on the figure, $\Delta f_1=-334.5$ kHz, $\Delta f_z=165.5$ kHz, $\Delta f_3=665.5$ kHz, other parameters are the same as in Fig. 11. (b) Fast Fourier transform for orbit in (a). (c) Computed Silnikov-type orbit for 3 modes. Only mode 3, the "weak mode," is shown. $P_{\mathrm{in}}=0.024\,29$ W, $\Delta f_1=-300$ kHz, $\Delta f_2=200$ kHz, $\Delta f_3=700$ kHz, other parameters are the same as Fig. 9. (d) Time series for this orbit.

variety previously described). Figures 12(c) and 12(d) show a case in which only the third mode is of the "weak" variety, while the other two modes are normally oscillating at a high level. The excitation which the weak mode receives from the pump and from the "strong" modes is just sufficient to allow it to grow at a slow rate from an initially very small amplitude. This growth may extend over several orders of magnitude in amplitude, lasting for a hundred cycles ore more of the strong mode oscillation. Finally, when the size of the orbit becomes comparable to the size of the strong mode orbits, a rapid interaction phase occurs involving all three modes and leads to the return of the weak mode to a very low amplitude and then the process repeats (approximately). This appears to be an orbit of the "Silnikov" or spiral saddle type (see Guckenheimer and Holmes[39]), for which the existence of "horseshoes" and other complex behavior have been explicitly shown.

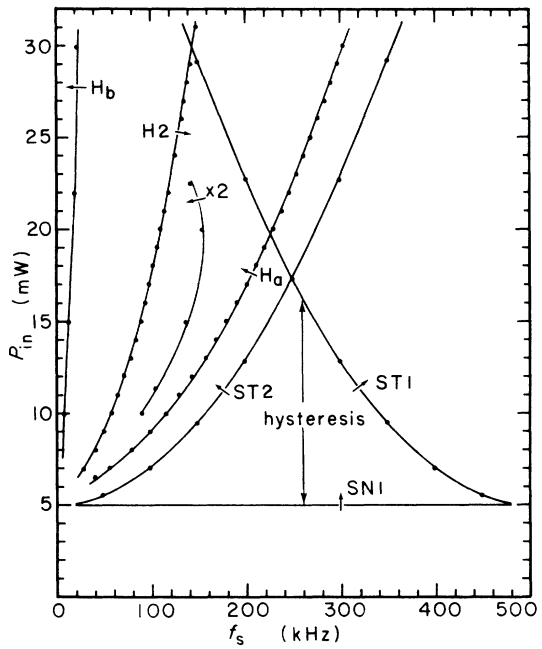

FIG. 13. Computed parameter-space diagram for mode series. Mode frequency shift f_s vs applied power P_{in} (shift corresponds to change of dc field in experiment). The dynamics involve the active participation of zero, one, two, or three modes. At higher powers than shown in the figure additional modes may become involved. We label the modes as follows: mode 1 has $\Delta f_1 = f_s - 500$ kHz, mode 2 has $\Delta f_2 = f_s$, mode 3 has $\Delta f_3 = f_s + 500$ kHz. ST1 and ST2 are the Suhl thresholds for excitation of modes 1 and 2, respectively, when all other modes are set to zero (this is actually a symmetry breaking bifurcation for the stable fixed point at zero). SN1 is a saddle-node bifurcation of nonzero fixed points below Suhl threshold [see Fig. 7(e)]. Hysteresis is observed when traversing the region between SN1 and ST1. Crossing H_a in the direction of the arrow a Hopf bifurcation occurs in which a limit cycle involving modes 1 and 2 emerges from a fixed point. This is of the type shown in Figs. 9(a) and 9(b). This oscillation undergoes a period-doubling bifurcation upon crossing the line labeled $\times 2$. Beyond this a cascade of period doublings occurs on route to chaos. On approach to the line H2, mode 3 becomes active and the two-mode solution we have been following is abruptly lost. H2 actually corresponds to a secondary Hopf bifurcation from a three-mode periodic orbit (on the left side) to a three-mode quasiperiodic orbit (on the right side), of the type shown in Fig. 11. H_b corresponds to another primary Hopf bifurcation, this time involving modes 2 and 3. Relaxation oscillations occur above the line ST1 in the section below its intersection with ST2. Onset appears to occur at the Suhl threshold ST1.

This representation of the system as a series of equally spaced modes may be taken to the limit of an infinite series. The reason that this procedure is valid is that only those modes with relatively small detuning can become excited and interact with the other excited modes. Modes which decay to zero have no effect on the excited modes. Thus we need to include in the computer simulation only those modes in the series with sufficiently small detuning (positive or negative) to become excited. The necessary number may be found by extending the series one mode at a time until the new modes added are observe to be inactive. Since the series is infinite, its behavior in parameter space is periodic with respect to synchronously shifting the frequencies by the mode spacing. In Fig. 13 one period of the computed parameter space diagram is shown. In this region, all of the types of behavior discussed previously may be found: stable fixed points (zero and nonzero), hystersis, auto-oscillations, period doubling, quasiperiodicity, chaos, and relaxation oscillations. Indeed, this figure and detailed caption aptly summarize the behavior of our model.

V. SUMMARY AND CONCLUSION

Excited spin waves in YIG form a weakly damped—nearly Hamiltonian—system, which displays a great variety of interesting nonlinear phenomena. This study focused on the behavior of spin waves excited parametrically at 9.2 GHz in a spherical sample via the first-order Suhl instability. The data are primarily for perpendicular pumping, and with the dc field parallel to the [111] or easy axis of the crystal, but with some data for other orientations of pumping and crystalline axes. The observed phenomena include (1) fine structure, the excitation of single spinwave modes; (2) dynamics in the fine-structure regime, involving the interaction of a small number (1,2,3,. . .) of spin-wave modes, these typically exhibit such phenomena as periodic auto-oscillations (typically 100 kHz), cascades of period doublings to chaos, and quasiperiodicity; (3) low-frequency relaxation oscillations (typically 1 kHz) and aperiodic spiking (typically at somewhat higher frequencies); (4) high-amplitude collective oscillations, presumably involving the cooperation of many modes, these exhibit period doubling, quasiperiodicity, phase locking of multiple frequencies, and various types of chaotic orbits; (5) abrupt emergence of high-frequency noise; (6) hysteresis at the Suhl threshold in which the system jumps from a quiescent to a turbulent state; and (7) in some cases, a systematic increase in auto-oscillation frequency with pumping power.

A first-principles theoretical analysis has been presented, based on the many earlier works on parametric exci-

tation of spin waves, but developed here explicitly for the study of the nonlinear dynamics of excited spin-wave modes. The theory explicitly includes the effects of crystalline and shape anisotropy. Also included are the interactions with the resonator (used to intensify the microwave field) and coupling to the waveguide. The overall result is a set of nonlinear equations [Eq. (65)] coupling the spin-wave modes with each other and with the pumping field, each mode being represented by a complex amplitude. A stability analysis has been made of the trivial and nontrivial fixed points of the equations of motion, and it has been shown how this can lead to hysteresis at the Suhl threshold, an effect which was observed in the experiment.

Some theory is presented regarding relaxation oscillations and aperiodic spiking behavior, based on the idea that there are weak modes which are only active during short burst phases, which may be instigated when the amplitude of a strong mode reaches a critical threshold. This type of oscillation provides a natural way for stochasticity to enter into the experimental dynamics because during the dormant phase of the weak mode it can easily decay to the thermal magnon level. After this the squbseuent dynamics become unpredictable. This analysis may be related to the work on irregular periods by Waldner *et al.*[20,38]

A detailed study is made of the behavior of the spin-wave equations of motion using numerical iteration. Many detailed similarities are found between these model calculations and the experimental data. A series of equally spaced (in frequency) modes is studied, similar to that which was observed experimentally. For two modes, autooscillations are observed which exhibit novel symmetry characteristics. Relaxation and spiking behaviors are also observed experimentally, exhibiting the behavior of interacting weak and strong modes discussed in the theory. Cascades of period-doubling bifurcations are observed, leading to chaos, in the experiment and in the model. For three modes quasiperiodicity is first observed, along with the phase-locking phenomena, Hopf bifurcations, and the quasiperiodic route to chaos, both in the experiment and in the model. Orbits nearly homoclinic to a spiral saddle point of the Silinkov type are also observed. The case of an infinite series of modes is also considered. It is possible to study this due to the fact that only a few modes in the series have sufficiently small detuning to be excited. The type of behavior is periodic under a synchronous shifting of all of the frequencies of the modes by the frequency spacing of the modes; this shifting corresponds to the effect of changing the dc field in the experiment. The model behavior is summarized by a parameter-space plot (pump power versus frequency shift) showing the locations of various bifurcations and behavior patterns. On the whole, the experimental behavior, believed to be generic, can be understood from the model. Both experiment and model have shown a great wealth of interesting dynamical phenomena.

ACKNOWLEDGMENTS

This work was supported in part by the Director, Office of Energy Research, Office of Basic Energy Sciences, Materials Sciences Division of the U.S. Department of Energy under Contract No. DE-AC03-76SF00098 and by the Office of Naval Research under Contract No. N00014-86-K-0154.

*Present address: Institute for Pure and Applied Physical Sciences, University of California, San Diego, La Jolla, CA 92093.

†Present address: James Franck Institute, University of Chicago, Chicago, IL 60637.

[1]R. W. Damon, Rev. Mod. Phys. **25**, 239 (1953).

[2]N. Bloembergen and S. Wang, Phys. Rev. **93**, 72 (1954).

[3]V. E. Zakharov, V. S. L'vov,and S. S. Starobinets, Usp. Fiz. Nauk **114**, 609 (1974) [Sov. Phys.–Usp. **17**, 896 (1975)].

[4]H. Suhl, J. Phys. Chem. Solids **1**, 209 (1957).

[5]George Gibson and Carson Jeffries, Phys. Rev. A **29**, 811 (1984).

[6]F. M. de Aguiar and S. M. Rezende, Phys. Rev. Lett. **50**, 1070 (1986).

[7]M. Mino and H. Yamazaki, Phys. Soc. Jpn. **55**, 4168 (1986).

[8]H. Yamazaki and M. Warden, Phys. Soc. Jpn. **55**, 4477 (1986).

[9]P. Bryant, C. Jeffries, and K. Nakamura, in Phys. Rev. Lett. **60**, 1185 (1988).

[10]P. Bryant, C. Jeffries, and K. Nakamura, in *The Physics of Chaos and Systems Far from Equilibrium,* edited by M. Duong-van and B. Nichols (North-Holland, Amsterdam, 1987), p. 25.

[11]Paul Henry Bryant, Ph.D. thesis, University of California, Berkeley, 1987, University of Microfilms International, Ann Arbor, Michigan.

[12]T. L. Carrol, L. M. Pecora, and F. J. Ratchford, Phys. Rev. Lett. **59**, 2891 (1987).

[13]K. Nakamura, S. Ohta, and K. Kawasaki, J. Phys. C **15**, L143 (1982).

[14]K. Nakamura, S. Ohta, and K. Kawasaki, J. Phys. Soc. Jpn. **52**, 147 (1983).

[15]S. Ohta and K. Nakamura, J. Phys. C **16**, L605 (1983).

[16]X. Y. Zhang and H. Suhl, Phys. Rev. A **32**, 2530 (1985).

[17]H. Suhl and X. Y. Zhang, Phys. Rev. Lett. **57**, 1480 (1986).

[18]S. M. Rezende, O. F. de Alcantara Bonfim, and F. M. de Aguiar, Phys. Rev. B **33**, 5153 (1986).

[19]X. Y. Zhang and H. Suhl, Phys. Rev. B **38**, 4893 (1988).

[20]F. Waldner, D. R. Barberis, and H. Yamazaki, Phys. Rev. A **31**, 420 (1985).

[21]D. Ruelle and F. Takens, Commun. Math. Phys. **20**, 167 (1971).

[22]A. M. Clogston, H. Suhl, L. R. Walker, and P. W. Anderson, J. Phys. Chem. Solids **1**, 129 (1956).

[23]Marshall Sparks, *Ferromagnetic Relaxation Theory* (McGraw-Hill, San Francisco, 1964).

[24]S. Geller, H. J. Williams, R. C. Sherwood, J. P. Remeika, and G. P. Espinosa, Phys. Rev. **131**, 1080 (1963).

[25]W. Froncisz and James S. Hyde, J. Magn. Reson. **47**, 515 (1982).

[26]W. Jantz and J. Schneider, Phys. Status Solidi **31**, 595 (1975).

[27]Paul H. Bryant (unpublished).

[28]V. V. Zautkin, V. S. L'vov,and S. S. Starobinets, Zh. Eksp. Teor. Phys. **63**, 182 (1972) [Sov. Phys.—JETP **36**, 96 (1973)].

[29]Ernst Schlomann, Phys. Rev. **116**, 828 (1959).

[30]V. E. Zakharov, V. S. L'vov, and S. S. Starobinets, Fiz. Tverd. Tela (Leningrad) **11**, 2047 (1969) [Sov. Phys.—Solid State **11**, 2368 (1970)].
[31]V. E. Zakharov, V. S. L'vov, and S. S. Starobinets, Zh. Eksp. Teor. Phys. **59**, 1200 (1970) [Sov. Phys.—JETP **32**, 656 (1971)].
[32]T. Holstein and H. Primakoff, Phys. Rev. **58**, 1098 (1940).
[33]Conyers Herring and Charles Kittel, Phys. Rev. **81**, 869 (1951).
[34]J. A. Osborn, Phys. Rev. **67**, 351 (1945).
[35]Edmund C. Stoner, Philos. Mag. **36**, 803 (1945).
[36]P. Hansen, J. Appl. Phys. **45**, 3638 (1974).
[37]P. Hansen, in *Physics of Magnetic Garnets,* edited by A. Paoletti (North-Holland, New York, 1978), p. 56.
[38]F. Waldner, R. Badii, D. R. Barberis, G. Broggi, W. Floeder, P. F. Meier, R. Stoop, M. Warden, and H. Yamazaki, J. Magn. Magn. Mat. **54-57**, 1135 (1986).
[39]J. Guckenheimer and P. Holmes, *Nonlinear Oscillations, Dynamical Systems, and Bifurcations of Vector Fields* (Springer, New York, 1983).
[40]Paul Bryant and Carson Jeffries, Physica D **25**, 196 (1987).
[41]M. J. Feigenbaum, L. P. Kadanoff, and S. J. Shenker, Physica D **5**, 370 (1982).
[42]S. Ostlund, D. Rand, J. Sethna, and E. Siggia, Physica D **8**, 303 (1983).

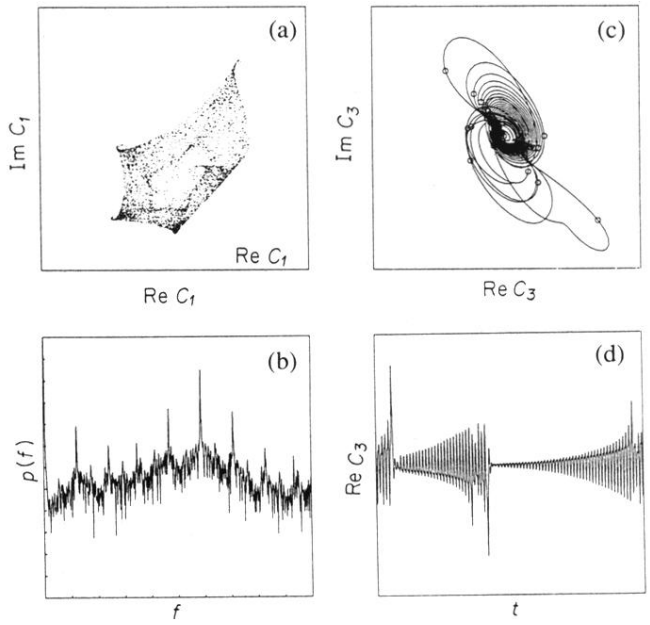

FIG. 12. (a) Poincaré section of chaotic orbit, following quasiperiodic transition to chaos. Proximity to period-5 locking produces five points on the figure, $\Delta f_1 = -334.5$ kHz, $\Delta f_z = 165.5$ kHz, $\Delta f_3 = 665.5$ kHz, other parameters are the same as in Fig. 11. (b) Fast Fourier transform for orbit in (a). (c) Computed Silnikov-type orbit for 3 modes. Only mode 3, the "weak mode," is shown. $P_{\text{in}} = 0.024\,29$ W, $\Delta f_1 = -300$ kHz, $\Delta f_2 = 200$ kHz, $\Delta f_3 = 700$ kHz, other parameters are the same as Fig. 9. (d) Time series for this orbit.

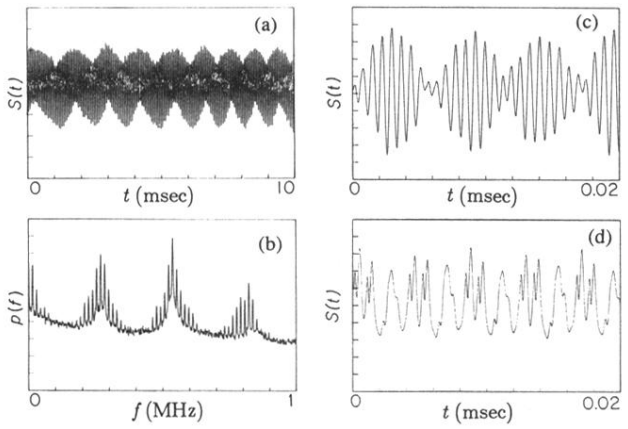

FIG. 5. (a) Observed ac signal of collective quasiperiodic oscillations of spin-wave instabilities in a YIG sphere. (b) Power spectrum of two-frequency quasiperiodic oscillations; 10 dB per division. (c) Two-frequency quasiperiodic oscillations for axis [100] parallel to H_0. (d) Frequency locking at period 14.